JACS
JOURNAL OF THE AMERICAN CHEMICAL SOCIETY
Perspective
pubs.acs.org/JACS

Direct Chemical Dynamics Simulations

Subha Pratihar,[†] Xinyou Ma,[†] Zahra Homayoon,[†] George L. Barnes,[‡] and William L. Hase*[,†]

[†]Department of Chemistry and Biochemistry, Texas Tech University, Lubbock, Texas 79409-1061, United States
[‡]Department of Chemistry and Biochemistry, Siena College, Loudonville, New York 12211, United States

ABSTRACT: In a direct dynamics simulation, the technologies of chemical dynamics and electronic structure theory are coupled so that the potential energy, gradient, and Hessian required from the simulation are obtained directly from the electronic structure theory. These simulations are extensively used to (1) interpret experimental results and understand the atomic-level dynamics of chemical reactions; (2) illustrate the ability of classical simulations to correctly interpret and predict chemical dynamics when quantum effects are expected to be unimportant; (3) obtain the correct classical dynamics predicted by an electronic structure theory; (4) determine a deeper understanding of when statistical theories are valid for predicting the mechanisms and rates of chemical reactions; and (5) discover new reaction pathways and chemical dynamics. Direct dynamics simulation studies are described for bimolecular S_N2 nucleophilic substitution, unimolecular decomposition, post-transition-state dynamics, mass spectrometry experiments, and semiclassical vibrational spectra. Also included are discussions of quantum effects, the accuracy of classical chemical dynamics simulation, and the methodology of direct dynamics.

1. INTRODUCTION

Classical chemical dynamics simulations[1,2] are an important tool that obtains atomistic level information for studying a broad range of chemical problems, including intermolecular collisional energy transfer, intramolecular vibrational energy flow, molecular motions and conformational changes, and unimolecular and bimolecular reactions. The earliest simulations were for unimolecular[3,4] and bimolecular[5,6] reactions; the same approach has now been applied to a wide range of problems including gas−surface energy transfer[7] and reactions,[8] post-transition-state (TS) dynamics,[9] intramolecular vibrational energy redistribution (IVR) in molecules,[10] and heat transfer across interfaces.[11] For such simulations, an ensemble of classical trajectories are calculated by numerically integrating either Newton's or Hamilton's classical equations of motion.[1,2] Each trajectory in the ensemble has a different initial condition, with specific values for the coordinates and velocities of the atoms for the chemical system under investigation. To illustrate, in numerically integrating Newton's equations of motion, $F_i = -\partial V/\partial q_i = m_i(d^2q_i/dt^2)$ is solved simultaneously for each Cartesian coordinate q_i at each numerical integration time step. Here, F_i is the force for q_i, $\partial V/\partial q_i$ is the derivative of the potential energy with respect to q_i, and d^2q_i/dt^2 is the acceleration for q_i. This numerical integration gives the motions of the atoms, following the initial condition, for the chemical system under study, i.e., the trajectory.

In order to compare with the prediction of a chemical dynamics theory or experiment, it is critical that accurate and appropriate initial conditions are chosen for the trajectories in the ensemble.[2] In modeling a bimolecular reaction, the quasiclassical trajectory (QCT) method is often used, in which initial conditions are sampled from the vibrational and rotational energy levels of the reactants.[1,6,12] For a bimolecular S_N2 nucleophilic substitution reaction, such as $Cl^- + CH_3Br \rightarrow ClCH_3 + Br^-$, the results obtained from the QCT simulation include the reaction rate constant versus temperature and collision energy, the effect on the reaction probability and rate constant of exciting specific CH_3Br vibrational modes, the relative importance of different atomistic reaction mechanisms (e.g., direct or indirect), and the manner in which the product energy is partitioned to translation, rotation, and vibration. To compare with the Rice−Ramsperger−Kassel−Marcus (RRKM) theory of unimolecular decomposition, which assumes complete IVR during the unimolecular reaction, a microcanonical ensemble of states is prepared for the unimolecular reactant's initial conditions.[3,4,13] The sampling of initial conditions is considered in more detail below in presenting specific direct dynamics studies. However, to illustrate the sampling of initial conditions, preparing a microcanonical ensemble for a vibrationally excited molecule and selecting vibrational energy levels at a TS are considered here.

For a microcanonical ensemble of a vibrationally excited molecule, each vibrational state in the energy interval $E \rightarrow E + \Delta E$ has an equal probability of being populated. Each state, for a nonlinear molecule, has a random energy E_i in each of the $3N - 6$ vibrational normal modes, with the sum of the E_i equal to E in the interval $E \rightarrow E + \Delta E$.[13] Sampling of initial conditions for a chemical dynamics simulation of a microcanonical ensemble, first involves choosing a vibrational state at random with mode energies E_i. A random phase is then chosen for each mode, transforming its E_i into a normal mode coordinate Q_i and momentum P_i. The normal mode eigenvector, determined by calculating the vibrational frequencies for the molecule, is then used to transform all the Q_i and P_i to Cartesian coordinates and momenta used to integrate the trajectory. With this sampling, a random set of initial conditions are chosen for the molecule, forming a microcanonical ensemble. If the ensemble's energy E is above the molecule's unimolecular threshold E_o, it will decompose. For RRKM unimolecular dynamics the relative number of molecules remaining in the ensemble at time t will decay exponentially

Received: November 21, 2016
Published: January 24, 2017

DOI: 10.1021/jacs.6b12017
J. Am. Chem. Soc. 2017, 139, 3570−3590

with the RRKM rate constant, i.e., $N(t)/N(0) = \exp(-kt)$, where $N(0)$ is the number of initial conditions for the ensemble. For non-RRKM dynamics, the decay is nonexponential.[3]

Direct dynamics simulations are also important for investigating post-TS dynamics after passing a rate controlling TS.[9] Included in the simulation results is energy partitioning for the reaction products and branching between multiple product pathways. For these simulations a Boltzmann distribution is prepared at the TS in accord with TS theory. For a nonlinear molecule there are the $3N - 7$ vibrational modes and the reaction coordinate at the TS. In selecting an initial condition for an ensemble of trajectories at the TS, the quantum Boltzmann distribution is sampled for each vibrational mode to determine its energy E_i, which is transformed into the mode's Q_i and P_i as described above. The reaction coordinate momentum P_{rc} is sampled from its classical Boltzmann distribution. The TS normal mode eigenvector is then used to transform the Q_i, P_i, and P_{rc} to the Cartesian coordinates and momenta used to integrate the trajectories. The sign of P_{rc} is used to direct the trajectories toward products from the TS.

The total energy for a chemical system is a sum of the atoms' kinetic and potential energies and, when solving either Newton's or Hamilton's equations of motion, the derivatives of the potential energy with respect to the atoms' coordinates, i.e., $\partial V/\partial q_i$ the gradient, is required. The traditional way to perform a classical dynamics simulations is to represent the potential energy, i.e., the potential energy surface (PES), by an analytic function.[1,3−6] This function could be a model, such as the London−Eyring−Polanyi−Sato (LEPS)[14] PES for atom + diatom reactions, or determined by fitting electronic structure calculations (ESCs).[15] This approach is still used extensively and major advances have been made in developing such analytic PESs.[16,17]

Another approach for performing a classical chemical dynamics simulation is direct dynamics, in which the trajectory is numerically integrated "on the fly" by obtaining the potential energy and its gradient directly from a quantum mechanical (QM) electronic structure theory.[18,19] The first study of this type involved calculating several trajectories for the $^1CH_2 + H_2 \rightarrow CH_4$ reaction with the CNDO electronic structure theory.[20] Several years later, the first *ab initio* direct dynamics trajectories were calculated for the $H^- + CH_4$ S_N2 reaction using HF/STO-3G theory.[21] Starting in the 1990s, direct dynamics simulations comprising ensembles of classical trajectories were first performed[22−27] and there are two flavors for these simulations.[19] For one, the trajectory is calculated "on the fly",[18] with the potential energy and gradient obtained directly from a QM theory with no need for an analytic potential energy function. Such calculations are referred to as QM direct dynamics. For some problems, particularly those with many atoms, part of the chemical system may be represented by molecular mechanical (MM) analytic potential energy functions so that the gradient is a sum of terms from both the QM theory and the MM function. This is referred to as QM/MM[28] or QM +MM direct dynamics.[19]

It is important to recognize that the direct dynamics simulations discussed here are also often referred to as first-principles dynamics,[29] Born−Oppenheimer molecular dynamics (BOMD),[30] and *ab initio* molecular dynamics (AIMD).[31] We prefer the direct dynamics terminology since it includes *ab initio*, density functional theory (DFT), and semiempirical electronic structure theories, as well as both QM and QM/MM dynamics. The term "direct dynamics" is also used at times to identify the calculation of the intrinsic reaction coordinate (IRC)[32] on a PES directly from a QM theory,[33] without the need for an analytic potential energy function. Finally, it is important to note the difference between the direct chemical dynamics simulations discussed here, for which an ensemble of trajectories are calculated, and a molecular dynamics (MD) simulation[34,35] for which a single trajectory is calculated. For this latter simulation the potential energy and its gradient may be determined directly from a QM theory as in direct dynamics. For the MD simulation it is assumed that the motion of the single trajectory is ergodic, so that it creates a proper ensemble of states;[36] as discussed below, a MD simulation may be used to generate initial conditions for a chemical dynamics simulation. If this single trajectory is coupled to a thermal bath, the properties of a constant temperature T canonical ensemble are obtained. For a large system, with many atoms, constant T properties may be found from a constant energy trajectory.

There are multiple motivations for direct dynamics simulations: they may be used to interpret experimental results and understand the atomic-level dynamics of chemical reactions; the simulations illustrate the ability of classical dynamics to correctly interpret experiments and predict chemical dynamics, when quantum effects are expected to be unimportant; with direct dynamics one obtains the classical atomistic dynamics predicted by a QM theory, in much the same way molecular structures, vibrational frequencies, and energies are obtained from QM theories; and the simulations provide a deeper understanding of when statistical theories are valid for predicting mechanisms and rates of chemical reactions. Finally, there is an exciting "discovery" component to direct dynamics, in that new reaction pathways and chemical dynamics are often discovered. Atomistic reaction mechanisms are often described in terms of a one-dimensional potential energy curve consisting of potential energy minima and TS stationary points, and IRCs connecting them. As discussed below, this is often an overly simplistic picture of the actual multidimensional atomistic dynamics. With direct dynamics, the actual chemical dynamics may be discovered. All of the above motivations are components of the direct dynamics simulations discussed below. However, before presenting this work, the accuracy of classical chemical dynamics and the methodology and enhancements of direct dynamics are considered.

2. ACCURACY OF CLASSICAL CHEMICAL DYNAMICS

2.1. Fundamentals. Actual chemical dynamics are quantal, not classical, and there may be quantum effects which make the classical dynamics inaccurate.[37] As described quite lucidly by Schatz,[38] "all quantum effects are interference effects". However, in comparisons with classical mechanics it is easier to use descriptions different than that of interferences to consider quantum effects. In particular, zero-point energy (ZPE), tunneling, and resonances are often important quantum effects.[38] For a classical chemical dynamics simulation of a bimolecular or unimolecular reaction, trajectories may cross the TS barrier and/or form products without ZPE in their vibrational modes. Classical dynamics allows ZPE to flow and "pool" within a molecule.[39,40]

These unphysical dynamics are illustrated by the unimolecular decomposition of a molecule which has rapid IVR and whose classical intramolecular dynamics is thus ergodic, so that its decomposition is intrinsically RRKM.[41] The molecule may

DOI: 10.1021/jacs.6b12017
J. Am. Chem. Soc. 2017, 139, 3570−3590

be excited randomly with a quasiclassical microcanonical ensemble of states,[13] so that each state in the energy interval $E \rightarrow E + \Delta E$ has the same probability of being populated. However, because of the classical ergodic dynamics, this quasiclassical ensemble will rapidly become a classical microcanonical ensemble, with ZPE randomized, and the trajectories will decompose in accord with classical RRKM unimolecular rate theory. Such dynamics have been described for $C_2H_5 \rightarrow H + C_2H_4$ dissociation on a PES with a classical dissociation barrier of 43.5 kcal/mol with respect to the potential energy minimum.[42] The quantal barrier includes ZPE at the TS and is 73.8 kcal/mol. Thus, excited C_2H_5 molecules with a total energy, including ZPE, between 43.5 and 73.8 kcal/mol dissociate classically, but in the absence of tunneling do not dissociate quantum mechanically.[43]

Motions associated with the reaction coordinate and vibrations at the barrier TS are not separable and, as a result, tunneling and ZPE at the barrier are nonseparable.[38] This "mixing" between tunneling and ZPE was discussed in a classical chemical dynamics study of the $H + C_2H_4 \rightarrow C_2H_5$ association reaction.[43] If it is assumed, as in transition state theory (TST), that the TS has ZPE, the quantum barrier for reaction is the vibrationally adiabatic ground-state barrier[37] and is used to identify tunneling.[44]

Resonances for bimolecular and unimolecular reactions may be viewed as localized wave packets composed of a superposition of continuum wave functions, which for a time qualitatively resemble bound states.[38] They are intermediate metastable states, with finite lifetimes corresponding to their dissociation. Primary quantum effects associated with resonances are their discrete energy level structure and their lifetimes. For a bimolecular reaction with an intermediate, such as HO_2 for the reaction $H + O_2 \rightarrow O + OH$, the resonances are temporarily trapped in the intermediate's well.[45] However, with rotational energy levels included, the state density for such intermediates is usually too high to observe the individual resonances and the statistical RRKM theory is often applicable for determining the intermediate's lifetime.

There are also resonances for bimolecular reactions, which do not have minima on their PESs. For these reactions, the resonances are understood by considering the vibrationally adiabatic potential energy curves for a chemical reaction.[46,47] These curves are created by following the reaction coordinate *rc* from the reactants to products and for each value of *rc* determining the vibrational energy levels for the $s - 1$ vibrational degrees of freedom orthogonal to *rc*, where $s = 3N - 6$ for nonlinear molecules. Each vibrational energy level is identified by a set of quantum numbers *n*. For a vibrationally adiabatic curve, the quantum number *n* for each of the $s - 1$ modes remains fixed in moving from reactants to products. The nature of a mode, as well as its vibrational frequency, may change during the course of the reaction. Shifting of the vibrational frequencies may give rise to minima, i.e., wells, along the *rc* and these minima are often in the TS region of the PES. Resonances may be localized within these minima. The state density for these resonances is often low and they have been observed in experiments and quantum dynamics calculations, which accurately represent the experiments.[48−50]

Unimolecular resonances are observed if the state density is not too high, as for van der Waals molecules[51] and the formyl radical HCO which dissociates to H + CO.[52] Unimolecular resonances may be viewed as an extension of bound states into the dissociative continuum, with their line widths broadened as a result of the Heisenberg uncertainty principle giving them their lifetimes. As for the bound states it may not be possible to assign quantum numbers to the resonance states, as a result of strong coupling between the vibrational modes. This is the case for HO_2 resonances,[45,53] while those for HCO are assignable.[53]

There are classical analogues to bimolecular and unimolecular resonances. The classical analogue for bimolecular resonances is temporary trapping of classical trajectories in the vibrationally adiabatic potential energy minima described above. The lifetime of a resonance may be associated with tunneling through a vibrationally adiabatic barrier, the stability of the periodic trajectory associated with the minimum in the vibrationally adiabatic potential energy curve, or a transition to a vibrationally adiabatic curve lower in energy.[54]

There is a classical-quantum correspondence for resonances to which quantum numbers may not be assigned, as well as to resonances for which quantum numbers may be assigned.[55] An example of the former is $HO_2 \rightarrow O + OH$ dissociation. Without rotational excitation, the state density of vibrationally excited HO_2 is sufficiently sparse that energies and line widths (i.e., lifetimes) may be determined for its resonance states.[56] The classical analogue for nonassignable unimolecular resonance levels are chaotic trajectories, giving rise to ergodic unimolecular dynamics. HO_2 has only three vibrational modes and ZPE conditions are less important, so that classical dynamics gives an accurate RRKM rate constant except very near the unimolecular dissociation threshold.[56] As discussed in the next section, there is a close relationship between the average unimolecular rate constant for the resonances and the classical trajectory unimolecular rate constant.[56]

For assignable resonances the intramolecular dynamics of the trajectories are not chaotic, which is illustrated by the resonances found for $HCO \rightarrow H + CO$ dissociation.[53] The energy for each resonance is above the unimolecular threshold and is identified by quantum numbers *n* for the H−C and C═O stretch and the HCO bend modes. The resonance states will have a small *n* for the H−C stretch, the dissociating coordinate, but may have quite large *n* for the C═O stretch and HCO bend modes. A classical trajectory may be initiated with fixed quanta in the three modes to represent the resonance state, and its motion may be quasiperiodic with no energy transfer between the modes[57] or semi-quasiperiodic with slow intramode energy transfer. For the former case the trajectory will have an infinite lifetime in contrast to the QM finite lifetime for the resonance state. For the latter, where there is energy transfer between the modes, an ensemble of trajectories representing the resonance state may give a lifetime in agreement with the QM value.

Though the above quantum effects are often important, as described previously,[9,58] "comparisons of classical dynamics simulations with experiments and quantum dynamics calculations have shown that trajectories give correct results for direct processes such as direct bimolecular reactions, unimolecular fragmentation on a repulsive potential energy curve, and short-time unimolecular decomposition and IVR. For these direct processes the unphysical flow and pooling of ZPE is less important and the classical dynamics tends to maintain the vibrational adiabaticity present in quantum dynamics." It is assumed that these dynamics occur in the absence of tunneling.

2.2. Illustrative Examples. Classical chemical dynamics simulations are widely used to study chemical reaction and energy transfer dynamics, and there have been numerous

DOI: 10.1021/jacs.6b12017
J. Am. Chem. Soc. 2017, 139, 3570−3590

comparisons between classical dynamics, quantum dynamics, and experiment. There is overall quite good agreement between classical and quantum dynamics, and experimental, reactive cross sections for the H(D) + $H_2(D_2)$[59−61] and F + $H_2(D_2)$ reactions.[62,63] For a range of polyatomic bimolecular reactions, classical and quantum dynamical rate constants are in quite good agreement.[64] In the following, several illustrative examples are given here of the agreement between classical dynamics and experiments and/or quantum dynamics for unimolecular and bimolecular reactions.

Above it is explained how the classical unimolecular kinetics for C_2H_5, with 15 vibrational degrees of freedom and ergodic unimolecular dynamics, is much different than the quantum unimolecular dynamics. However, there are molecules and excitation processes, which involve much fewer degrees of freedom, for which the classical dynamics agrees with the quantum dynamics and/or experiment. Two examples are $HO_2 \rightarrow H + O_2$ dissociation, excited with a microcanonical ensemble of its vibrational states,[56] and dissociation of Cl^----CH_3Cl formed by $Cl^- + CH_3Cl$ association.[65,66] For these dissociations, with few vibrational degrees of freedom, the ZPE problem described above for C_2H_5 dissociation is less important.

A fundamental comparison between classical and quantum unimolecular dynamics is for $HO_2 \rightarrow H + O_2$ dissociation. The classical dynamics is ergodic (i.e., intrinsically RRKM), in that a microcanonical ensemble of states in the classical phase space dissociates exponentially with the classical RRKM rate constant. Quantum vibrational levels of HO_2, excited above the unimolecular threshold, dissociate via resonance states whose energies may not be identified by quantum numbers for the HO_2 three vibrational degrees of freedom. This is consistent with the classical ergodic and RRKM dynamics found for HO_2 dissociation. The correspondence between the HO_2 quantum and classical unimolecular dynamics is that the average of the resonance rate constants k_i, for a small energy interval ΔE, agrees with the classical trajectory rate constant for the middle of the energy interval.[56]

Classical chemical dynamics simulations and experiment have compared the Cl^----CH_3Cl unimolecular kinetics. Cl^----CH_3Cl is formed by $Cl^- + CH_3Cl$ association, and both experiments and simulations show that only the three intermolecular modes of Cl^----CH_3Cl complex are excited by this association.[65−68] Experimental and simulation lifetimes of the complex are compared in Figure 1 and are in excellent agreement.

Two exemplary classical chemical dynamics simulations of bimolecular reactions, illustrating agreement with experiment, are the $OH^- + CH_3I$ and $O(^3P) + C_2H_4$ reactions. The former is a direct dynamics simulation[69,70] and discussed in more detail in a following section. The simulations were performed at the B97-1/ECP/d level of theory, which gives the potential energy curve for the reaction shown in Figure 2. As shown in Tables 1 and 2, for both the branching between the I^- S_N2 and CH_2I^- proton transfer products, and the overall reaction rate constant, the simulations give results in quantitative agreement with the temperature-dependent experiments.

For the $O(^3P) + C_2H_4$ reaction intersystem crossing (ISC), which couples the triplet PES with a singlet PES, is important. Bowman and co-workers developed analytic PESs for the triplet and singlet surfaces, including their spin−orbit coupling.[71] They then used these PESs in a chemical dynamics simulation of the $O(^3P) + C_2H_4$ reaction, with surface hopping between the triplet (T_1) and singlet (S_0) surfaces included to account for the ISC electronic non-adiabatic dynamics. The T_1 and S_0 potential energy curves, as well as the region for ISC, are depicted in Figure 3. Products are formed on both the T_1 and S_0 PESs, and the calculated distribution for the different products is in quite good agreement with experiment as shown in Table 3.

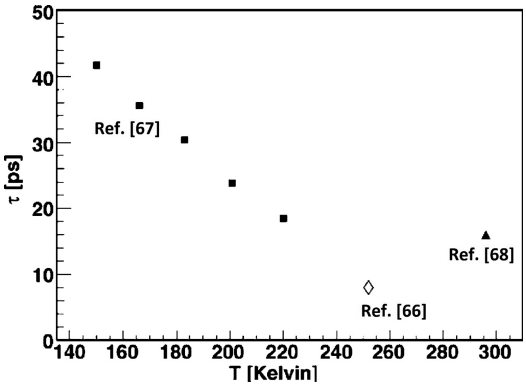

Figure 1. Average lifetime of the Cl^----CH_3Cl complex, extracted from the $Cl^- + CH_3Cl \rightarrow Cl^-$---$CH_3Cl$ ternary rate constant.[67] Included are values determined by high-pressure mass spectrometry[68] and chemical dynamics simulations.[66] Reproduced from ref 67 with permission from the American Chemical Society.

3. METHODOLOGY AND ENHANCEMENTS OF DIRECT DYNAMICS

The methodology of direct dynamics simulations is discussed in refs 72−74. Software for a direct chemical dynamics simulation requires both the chemical dynamics component (for choosing the trajectory initial conditions,[75,76] integrating the classical equations of motion,[77] and determining the trajectory final conditions[78]) and an electronic structure QM theory component. A practical approach for direct dynamics is to develop an interface that couples the chemical dynamics and QM components, with the latter providing the potential energies, gradients, and Hessians enabling the direct dynamics. Following this approach, the chemical dynamics code VENUS has been coupled with Gaussian,[79] NWChem,[69] and MOPAC.[25] For VENUS/NWChem[80] there is tight coupling between the two codes. They are compiled and linked together to act as one executable file with data being passed between the two codes through routine calls during a simulation. This is in contrast to loose coupling where the two codes execute relatively independent of one another.

The direct dynamics simulations presented and discussed here are Born−Oppenheimer (BO) direct dynamics[72−74] in which the time-independent Schrödinger equation is solved at each trajectory integration step or interpolated to a desired accuracy as described below. The Car−Parrinello (CP) method[72−74,34] is another approach for direct dynamics, which avoids the explicit electronic structure calculation (ESC) at each integration step by introducing a fictitious classical dynamics for the electronic wave function and corresponding fictitious electronic mass parameter μ. As described previously,[74] initially[34] it was thought that a CP direct dynamics simulation is substantially more computationally efficient that the BO approach, since it does not require an ESC at each integration step. However, detailed analyses (see discussion in ref 74) have shown that CP direct dynamics only recovers BO direct dynamics in the limit $\mu \rightarrow 0$ and a quite

DOI: 10.1021/jacs.6b12017
J. Am. Chem. Soc. 2017, 139, 3570−3590

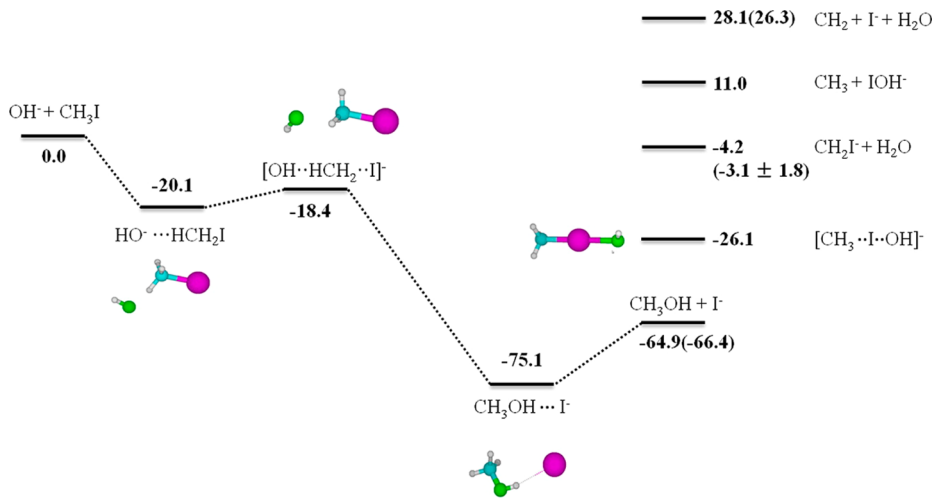

Figure 2. Schematic energy profile for the $OH^- + CH_3I \rightarrow CH_3OH + I^-$ S_N2 reaction at the DFT/B97-1/ECP/d level of theory, and other possible reaction channels. The energies shown are in kcal/mol and relative to the $OH^- + CH_3I$ reactants. Zero point energies are included. Experimental 0 K heats of reaction are in parentheses. Reproduced from ref 69 with permission from the American Chemical Society.

Table 1. Comparison of the Experiment and Simulation Temperature Dependence of the Anion Product Ratio for the $OH^- + CH_3I$ Reaction[a,b]

temp (K)	CH_2I^-	$[CH_3\text{--}I\text{--}OH]^-$	I^-	I^- (exp)	CH_2I^- (exp)
210				0.64	0.36
300	0.43 ± 0.05	0.03 ± 0.01	0.54 ± 0.06	0.56	0.44
400	0.45 ± 0.04	0.01 ± 0.01	0.54 ± 0.04	0.51	0.49
500	0.48 ± 0.06	0.05 ± 0.01	0.47 ± 0.05	0.46	0.54

[a]Results from ref 70. [b]Experimental branching error estimated to be 0.03 relative and 0.05 absolute.

Table 2. Comparison of the Experiment and Simulation Temperature Dependence of the $OH^- + CH_3I$ Rate Constant and the Calculated Collision Rate Constant[a,b]

	rate constant (cm^3/s)		
temp (K)	simulation	exp	calc coll
210		2.3×10^{-9}	3.0×10^{-9}
300	$(1.8 \pm 0.1) \times 10^{-9}$	1.7×10^{-9}	2.7×10^{-9}
400	$(1.8 \pm 0.1) \times 10^{-9}$	1.9×10^{-9}	2.5×10^{-9}
500	$(1.7 \pm 0.1) \times 10^{-9}$	1.8×10^{-9}	2.3×10^{-9}

[a]Results from ref 70. [b]Errors in the experimental rate constants are estimated to be ±25%.

small value for μ is needed to obtain accurate results. With such a small μ, a small integration step size is required and CP direct dynamics is not more efficient than BO direct dynamics. With BO direct dynamics one is assured of obtaining the correct classical dynamics from the electronic structure theory.

Direct dynamics simulations are computationally expensive and it is important to determine methods to make the simulations more efficient. One approach is to interpolate the ESC so that it does not need to be performed at each integration step. A method for doing this is suggested by using the potential energy, gradient, and Hessian at the current kth step of the integration to construct a local quadratic PES.[81,82] The trajectory is then integrated on this PES within a small trust radius. The integration within the trust region needs to be performed with an algorithm that conserves angular momentum. This method is not faster than a standard gradient-based

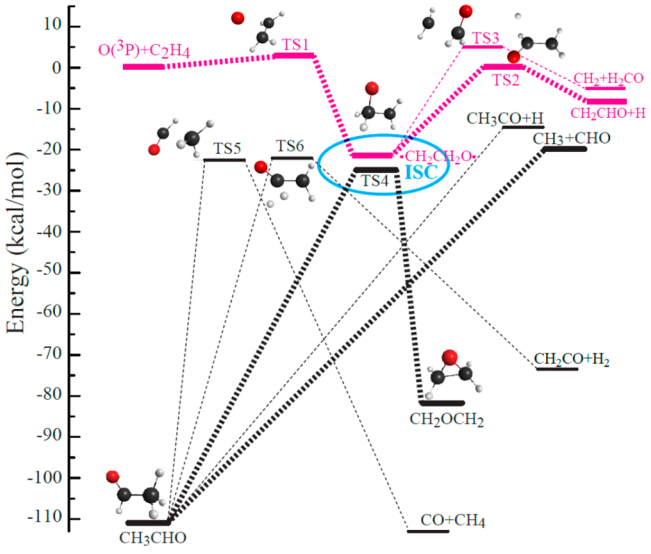

Figure 3. Schematic of triplet (red) and singlet (black) potential energy surfaces used in trajectory surface hopping simulations of the $O(^3P) + C_2H_4$ reaction. The biradical region, enclosed by the ellipse, is where the majority of the surface hops occur. Reproduced from ref 71 with permission from the National Academy of Sciences.

Table 3. Comparison between Simulation and Experimental Product Fractions for $O(^3P) + C_2H_4$ Reaction at a Collision Energy of 8.4 kcal mol^{-1}

product channel	theory[a]	experiment[a]
CH_3 + CHO (from S_0)	0.49	0.34 ± 0.09
CH_2CHO + H (from T_1)	0.28	0.30 ± 0.06
H_2CO + CH_2 (from T_1)	0.08	0.20 ± 0.05
CH_3CO + H (from S_0)	0.10	0.03 ± 0.01
CH_2CO + H_2 (from S_0)	0.05	0.13 ± 0.04

[a]Results from ref 71.

integration. However, it may be considered as a predictor step, which is then followed by a corrector step.[83−86] This predictor−corrector integrator constructs (interpolates) a local PES that is fifth order along the displacement of the trajectory for each time step and a large integration time step

DOI: 10.1021/jacs.6b12017
J. Am. Chem. Soc. 2017, 139, 3570−3590

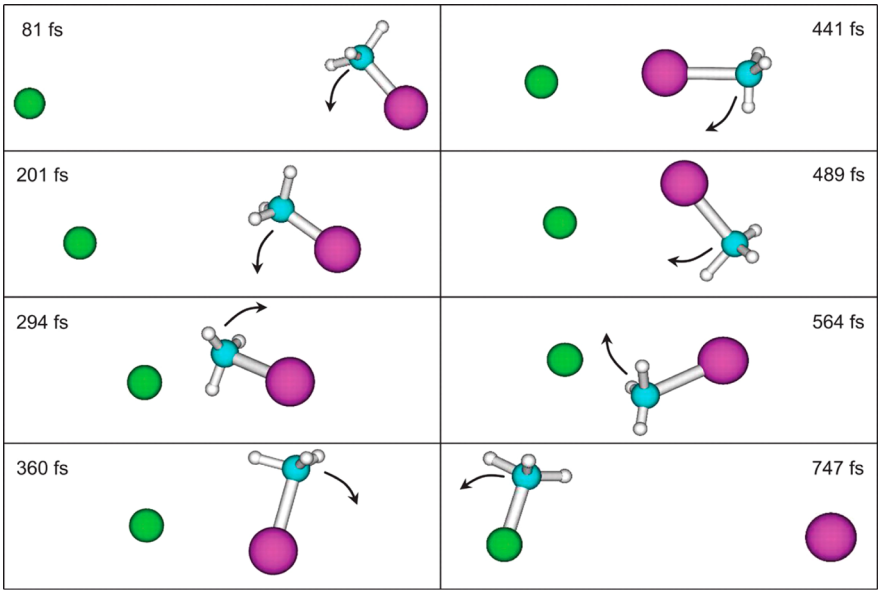

Figure 4. View of a typical trajectory for the indirect roundabout mechanism at a collision energy of 1.9 eV that proceeds via CH_3 rotation. Reproduced from ref 93 with permission from the American Academy for the Advancement of Science.

may be taken. These integrators reduce the number of ESCs needed to integrate the classical trajectory. However, this potential enhancement of the trajectory may be thwarted by the cost to obtain the Hessian. Tests are needed to determine the balance between the reduced number of ESCs and the cost of the Hessian.

The efficiency of the above algorithm may be greatly improved by using a Hessian update (interpolation) scheme in which an ESC is only performed every k integration steps. The traditional update scheme[87,88] is based on a first-order Taylor expansion for which the Hessian at point X_2 is

$$H(X_2)(X_2 - X_1) = G(X_2) - G(X_1) \quad (1)$$

This is a first-order expansion of the gradient $G(X_1)$ about X_2 and has a second-order error in $\|X_1 - X_2\|$. A more accurate update scheme, which has a third-order error in $\|X_1 - X_2\|$, is based on compact finite difference (CFD),[89] for which

$$\frac{1}{2}[H(X_1) + H(X_2)](X_2 - X_1) = G(X_2) - G(X_1) \quad (2)$$

Extensive tests have been made of the CFD scheme as compared to the first-order Taylor expansion and CFD is much more efficient and accurate.[90] It is expected that in the future new approaches and algorithms will be developed for interpolating the PES and enhancing direct dynamics simulations.

4. DIRECT CHEMICAL DYNAMICS SIMULATIONS

4.1. Bimolecular S_N2 Nucleophilic Substitution. Direct dynamics simulations have had a major impact on our understanding of the atomistic dynamics of gas-phase bimolecular $X^- + CH_3Y \rightarrow XCH_3 + Y^-$ S_N2 nucleophilic substitution reactions.[58,91,92] Overall, the simulation results are in excellent agreement with experiment. Comparisons with experiments of the Wester[93] and Viggiano[70] research groups are particularly important. The traditional mechanism for these reactions involves the formation of X^----CH_3Y pre-reaction and XCH_3---Y^- post-reaction complexes, with an intermediate $[X$--CH_3--$Y]^-$ central barrier for transferring the electron.[58,94] The complexes are assumed to have rapid IVR and RRKM unimolecular kinetics. Before the direct dynamics simulations were performed, it was known that S_N2 reactions may have important non-RRKM dynamics and the above statistical model was an oversimplification.[65,95−97] However, the direct dynamics simulations have confirmed the complexity of the S_N2 reactions, and shown that they are "rich" in atomistic and mechanistic detail.

Direct dynamics simulations were performed for Cl^-, F^-, OH^- and the microsolvated ions $F^-(H_2O)$ and $OH^-(H_2O)$ reacting with CH_3I. A representative potential energy curve for the unsolvated S_N2 reaction is shown in Figure 2. The simulations showed that the S_N2 reaction may occur by two direct mechanisms, rebound and stripping, and multiple indirect mechanisms.[91] For the rebound mechanism the colliding anion strikes the backside of CH_3I and the S_N2 molecular product rebounds off I^- in the backward direction. In contrast, for the stripping mechanism the colliding anion strips CH_3 from I^- and the molecular product scatters in the forward direction. The first reaction studied by direct dynamics is Cl^- + CH_3I, yielding an exciting new finding.[93] In agreement with molecular beam, ion imaging experiments, the simulations show that, as the collision energy E_{rel} of the reactants is increased, the reaction changes from an indirect mechanism with Cl^----CH_3I pre-reaction complex formation to a predominant direct mechanism, with rebound scattering.[98] The transition from the indirect reaction to a predominant direct reaction occurs over a very small E_{rel} range, a result found previously for Cl^- + CH_3Br with an analytic potential.[99] At the high collision energy of 1.9 eV the experimental scattering has attributes of an indirect mechanism. Pre-reaction complex formation is unexpected at this high collision energy and the origin of this unusual scattering was unclear. The simulations showed that this indirect mechanism occurs by a roundabout mechanism, previously unknown, involving CH_3 rotation. For this mechanism, depicted in Figure 4, Cl^- first strikes the side of the CH_3 group, causing it to rotate around the massive I atom. The collision also excites the C−I vibration. Then, after one CH_3 revolution, Cl^- attacks the C atom backside and directly

DOI: 10.1021/jacs.6b12017
J. Am. Chem. Soc. 2017, 139, 3570−3590

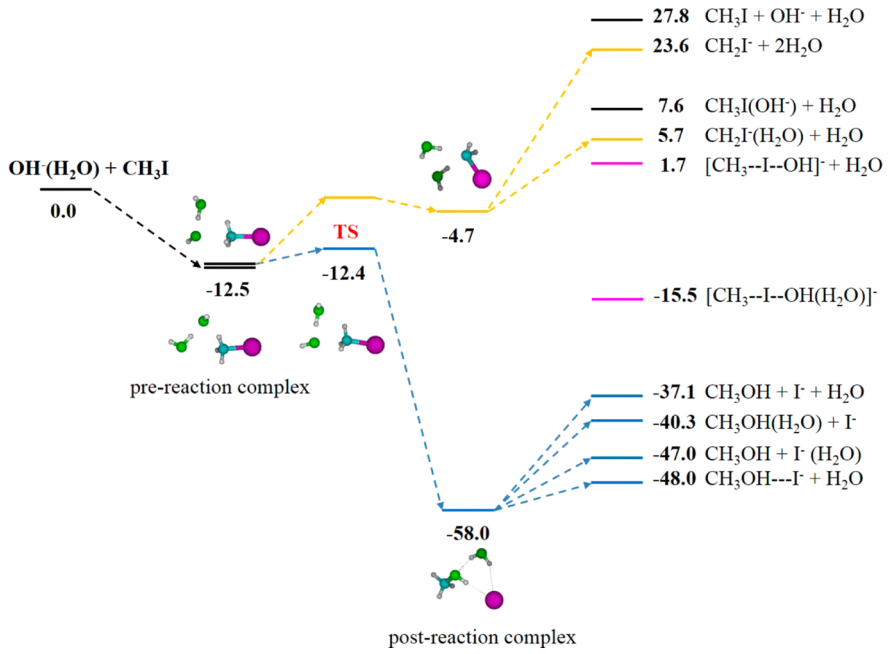

Figure 5. Schematic energy profile for the $OH^-(H_2O) + CH_3I \rightarrow CH_3OH + I^- + H_2O$ S_N2 reaction, and other pathways, at the DFT/B97-1/ECP/d level of theory. The energies shown are in kcal/mol and are relative to the $OH^-(H_2O) + CH_3I$ reactants. Zero point energies are included. Reproduced from ref 106 with permission from the American Institute of Physics.

displaces I^-. Of much less importance is substitution after CH_3 rotates twice about the I atom.

Direct dynamics were performed for the $F^- + CH_3I$ reaction using two electronic structure methods B97-1 and MP2, with the ECP/d basis set.[100−104] The majority of the simulations were performed with B97-1 at the collision energies E_{rel} of 0.32 and 1.53 eV.[100,101,104] For this reaction the S_N2 barrier is substantially submerged.[101] The B97-1 PES has a hydrogen-bonded F^----HCH_2I pre-reaction complex with a well depth of 20.2 kcal/mol and a very low barrier of 2.4 kcal/mol to reach the $[F--HCH_2I--I]^-$ S_N2 TS. In addition to these two stationary points, MP2 also has the traditional ion-dipole F^----CH_3I pre-reaction complex and a very low barrier TS connecting the hydrogen-bonding and ion−dipole pre-reaction complexes. The MP2 potential energies for these two complexes are similar and also similar to the potential energy for the B97-1 hydrogen-bonded complex. CCSD(T) calculations indicate the MP2 PES with the two pre-reaction complexes is correct.[103] However, the overall shapes of the B97-1 and MP2 pre-reaction PESs are similar.

The B97-1 direct dynamics at E_{rel} = 0.32 eV are in quite good agreement with the product energy and velocity scattering angular distributions measured in the molecular beam, ion imaging experiments.[100,101] The simulations show that the reaction occurs via the direct rebound and stripping mechanisms and an indirect mechanism with formation of the hydrogen-bonded F^----HCH_2I complex; the fractions of these three mechanisms are 0.15:0.25:0.60. The agreement between the B97-1 direct dynamics and experiment is not as good at E_{rel} of 1.53 eV. Classical dynamics is expected to be accurate for this exothermic reaction at high E_{rel} and the difference between simulation and experiment must arise from an inaccurate B97-1 PES at high energies.

A MP2 direct dynamics was performed for E_{rel} = 1.53 eV to see if better agreement with experiment was obtained.[102] MP2 and B97-1 give nearly identical average product energies, which agree with experiment, but MP2 gives a velocity scattering angle distribution in much better agreement with experiment. The fractions of the B97-1 and MP2 atomistic mechanisms are much different at E_{rel} = 1.53 eV. For B97-1 the fractions for the direct rebound and stripping and complex formation indirect mechanisms are 0.29:0.12:0.59, while these fractions are 0.46:0.43:0.11 for MP2. Direct reaction is much more important for MP2. It is somewhat surprising that, while B97-1 and MP2 give much different atomistic dynamics, they yield the same product energy distributions! B97-1 gives reaction rate constants for E_{rel} of 0.32 and 1.53 eV which agree with experiment, while the MP2 rate constant at E_{rel} = 1. 53 eV is a factor of 4 too low. The simulations illustrate that the B97-1 and MP2 PESs are different, but it is not clear which is more accurate.

As discussed above and shown in Tables 1 and 2, B97-1 gives accurate thermal rate constants and S_N2/proton transfer branching ratios for the $OH^- + CH_3I$ reaction.[70] The simulations were also performed for E_{rel} of 0.5−2.0 eV to compare with molecular beam, ion imaging experiments.[69] For these collision energies the S_N2 pathway occurred by the direct rebound and stripping mechanisms and seven different indirect mechanisms. Proton transfer had similar mechanisms. Both the S_N2 and proton transfer pathways were dominated by the stripping mechanism. At the lower thermal energies in Tables 1 and 2, the two direct mechanisms and the indirect mechanisms have nearly equal contributions for the S_N2 pathway, while the majority of the reaction is indirect for proton transfer. The simulation results are in good agreement with the molecular beam, ion imaging experiments for the proton-transfer pathway. However, for the S_N2 reaction, the experimental scattering is isotropic in nature whereas forward scattering dominates the simulation. The implication is that the simulations give too much stripping, which leads to forward scattering. Apparently, there are shortcomings in the B97-1 PES for the $OH^- + CH_3I$

DOI: 10.1021/jacs.6b12017
J. Am. Chem. Soc. 2017, 139, 3570−3590

reaction. The simulation dynamics for the OH^- + CH_3I S_N2 pathway are similar to those for F^- + CH_3I.

Direct dynamics simulations were used to study $OH^-(H_2O)$ + CH_3I[105−108] and $F^-(H_2O)$ + CH_3I[109] to investigate how microsolvation affects the X^- + CH_3Y reaction. Solvating the reactant anion adds considerable complexity to the reaction as illustrated by the $OH^-(H_2O)$ + CH_3I potential energy curve in Figure 5; e.g., there are four S_N2 pathways with different solvation motifs. The $OH^-(H_2O)$ + CH_3I direct dynamics were performed with the B97-1/ECP/d theory.[106] The S_N2 reaction dominates at all reactant collision energies and temperatures, and the reaction occurs by direct rebound and stripping mechanisms and 28 different indirect atomistic mechanisms. The latter dominates the reaction dynamics, and important indirect mechanisms are the roundabout and formation of S_N2 and proton transfer pre-reaction complexes and intermediates, including $[CH_3$--I--$OH]^-$.[108] In contrast, for the unsolvated OH^- + CH_3I S_N2 reaction, there are only seven indirect atomistic mechanisms and the direct mechanisms dominate. Microsolvation enhances indirect dynamics. The simulation results for the $OH^-(H_2O)$ + CH_3I S_N2 reaction are in good agreement with experimental measurements of the reaction rate constant and product branching ratio versus temperature.[107] The simulations are also in overall good agreement with the molecular beam, ion imaging experiments of the product energies and velocity scattering angle distributions.[106]

The $[CH_3$--I--$OH]^-$ and $[CH_3$--I--$OH]^-(H_2O)$ intermediates, and the pre-reaction complexes, may have isolated resonances[110,111] which should be possible to observe experimentally. It would be of much interest to use direct dynamics to search for the classical analogues[57] of these quantum resonances.

An important finding from the $OH^-(H_2O)$ + CH_3I microsolvation study is that equilibrium solvation by the H_2O molecule is unimportant.[106] The S_N2 reaction is dominated by events in which H_2O leaves the reactive system as CH_3OH is formed or before CH_3OH formation. Participation of the $(H_2O)CH_3OH$---I^- post-reaction complex for the S_N2 reaction is negligible. For simulations at a 0.05 eV collision energy, corresponding to a temperature of 387 K, the $I^-(H_2O)/I^-$ product ratio is 0.02. There are two origin of the suppressed formation of the solvated $I^-(H_2O)$ product. For trajectories that formed the $(H_2O)HO^-$---CH_3I pre-reaction complex, there is a strong propensity for H_2O dissociation from this complex as a result of the potential energy release in its formation. In addition, trajectories that crossed the S_N2 central barrier, with H_2O attached, did not follow the IRC to the post-reaction potential energy minima for $(H_2O)CH_3OH$---I^-. Instead they tended to follow a non-IRC pathway directly forming $[CH_3OH + I^- + H_2O]$ as a result of potential energy release as the reactive system moved from the central barrier to products.

Similar dynamics are found in direct dynamics simulations of the microsolvated S_N2 reaction $F^-(H_2O)$ + CH_3I at a 0.32 eV collision energy.[109] The water molecule preferentially leaves the reactive system before traversing the postreaction region of the PES.

4.2. Unimolecular Dissociation. Direct dynamics simulations may be used to study atomistic details of unimolecular reactions and compare with experiment and theoretical models such as RRKM theory. As discussed above, if the vibrational energy within the molecular reactant is randomly distributed, only in the high energy limit will its decomposition rate constant agree with experiment. This is a result of the unphysical flow of ZPE. However, if the molecule is excited nonrandomly, with its energy initially localized, its initial unimolecular and intramolecular dynamics, before extensive ZPE flow, may agree with experiment.

Direct dynamics of simulations of unimolecular reactions are also quite useful for identifying decomposition mechanisms and determining Arrhenius parameters. Finding all unimolecular reaction paths for a large molecule at high energy, by standard electronic structure methods, may be difficult. From direct dynamics simulations it was found that (1) protonated diglycine and octaglycine, colliding with a diamond surface at 100 eV, have 88 and 304 fragmentation pathways, respectively;[112,113] (2) the epoxy resin constituent CH_3−NH−CH═CH−CH_3 has 33 decomposition pathways at 3500−5500 K;[114] and (3) the doubly protonated tripeptide threonine-isoleucine-lysine ion, $TIK(H^+)_2$, randomly excited at 2500 K has 61 fragmentation pathways.[115]

In the following, several direct dynamics simulations of unimolecular decomposition, following nonrandom excitation and random thermal excitation, are discussed.

4.2.1. Dissociation following Nonrandom Excitation. Direct dynamics simulations of unimolecular decompositions for organic reactions, following nonrandom excitation, are summarized in Table 4.[116−133] For some reactions there is a reaction intermediate following a rate-controlling TS on the PES, and the intramolecular and unimolecular dynamics may be

Table 4. Non-random Excitation and Post-TS/Unimolecular Direct Dynamics Simulations of Nonstatistical Organic Reaction Dynamics

system	theory	year, ref
nonstatistical dynamics for a [1,3] sigmatropic migration	PM3	1995, 116
cyclopropane stereomutation and trimethylene unimolecular dynamics	AM1-SRP	1996, 117; 1997, 118; 1998, 119
nonexponential unimolecular decay for a reaction intermediate	AM1, PM3	1996, 120
biradical unimolecular dynamics for vinylcyclopropane → cyclopentene	AM1-SRP	2002, 121
unimolecular dynamics of 1,2,6-heptatrience rearrangement	CASSCF(8,8) AM1-SRP	2002, 122
methyl loss from the acetone radical cation	AM1-SRP	2002, 123
propene ozonolysis and dissociation of molozonide, forming the Criegee intermediate	B3LYP/6-31G*	2006, 124
nonstatistical dynamics in a carbene Wolff rearrangement	DFT/3-21G	2008, 125
unimolecular dynamics of the twist-boat intermediate for cyclohexane isomerization	HF/6-31G	2009, 126
alkene hydroboration	B3LYP/6-31G*	2009, 127
unimolecular dynamics of chemically activated cyclopentadiene	BS-UO3LYP/3-21G	2011, 128
nonstatistical dynamics in the ozonolysis of vinyl ethers	DFT/PDDG/PM3	2011, 129
simulation of dioxetane formation and decomposition	UB3LYP/6-31G*	2012, 130
mechanism of thiolate−disulfide exchange	PBE0/6-31+G*	2012, 131
activation and dissociation of 1,5-dinitrobiuret (HDNB)	M05-2X/6-31++G**	2014, 132
betaines as bypassed intermediates in solvent dynamics	M06-2X/6-31G* and 6-31+G**	2014, 133

DOI: 10.1021/jacs.6b12017
J. Am. Chem. Soc. 2017, 139, 3570−3590

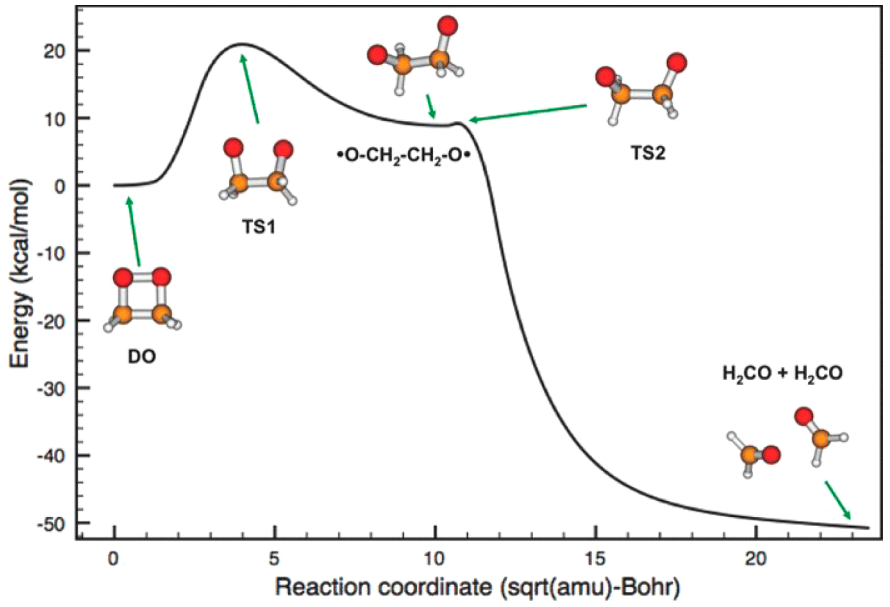

Figure 6. UB3LYP//6-31G* potential energy along the IRC for dissociation of dioxetane. Reproduced from ref 130 with permission from the American Institute of Physics.

studied by initiating the trajectories at this TS as described below in the Post-TS Dynamics section. Post-TS/unimolecular dynamics studies are included in Table 4. Below, the studies for dioxetane, the acetone radical cation, and the ozonolysis of vinyl ethers are discussed.

Direct chemical dynamics simulations were used to study the formation and decomposition of dioxetane on its ground state singlet PES.[130] The stationary points for this surface are $^1O_2$ + C_2H_4, the singlet $^\bullet O-O-CH_2-CH_2{}^\bullet$ biradical, the TS connecting this biradical with dioxetane, and the two TSs and gauche $^\bullet O-CH_2-CH_2-O^\bullet$ biradical connecting dioxetane with the formaldehyde product molecules, which were investigated at different levels of electronic structure and a range of basis sets. The potential energy curve for dioxetane dissociation to the formaldehyde products is depicted in Figure 6. The UB3LYP/6-31G* method was found to give representative energies for the reactive system and used for direct dynamics simulations in which ensembles of trajectories were initiated at the TS connecting the $^\bullet O-O-CH_2-CH_2{}^\bullet$ biradical and dioxetane with 300, 1000, and 1500 K distributions of energy. The TS's vibrational energy levels, and rotational and reaction coordinate energies, with Boltzmann distributions at 300, 1000, and 1500 K. The dioxetane molecules which are formed dissociate to two formaldehyde molecules with a rate constant 2 orders of magnitude smaller than that predicted by RRKM theory. Important nonstatistical dynamics are exhibited for this reactive system. There may be a bottleneck for IVR between the in-plane and out-of-plane modes of dioxetane as found molozonide.[124]

In the following two direct dynamics simulations, comparisons are made with experimental studies. Non-RRKM dynamics has been observed[123,134] for the isomerization of the acetone−enol cation $CH_3-COH-CH_2{}^+$ to the acetone cation $CH_3-CO-CH_3{}^+$, which then dissociates to $CH_3{}^+$ + CH_3CO and to CH_3CO^+ + CH_3. What is found from the simulations is that the methyl group formed by this isomerization is 1.36 ± 0.15 times more likely to dissociate from the acetone cation, which agrees with the experimental finding. In contrast, RRKM theory predicts equal dissociation probabilities for the two $-CH_3$ groups.

Non-RRKM and nonstatistical dynamics were found in chemical dynamics simulations of the ozonolysis of vinyl ethers, the results of which explain experimental observations.[129] The unimolecular dynamics of the primary ozonide, formed by the 1,3-dipolar addition of ozone to the vinyl ether, is nonstatistical. The unimolecular kinetics of the ozonide were determined both experimentally and computationally, versus the size of the alkyl group of the vinyl ether, and the effect of the alkyl group size was found to be much less than the prediction of RRKM theory. IVR for the primary ozonide is incomplete and does not involve all of its vibrational modes on the time-scale of its unimolecular decomposition. These results are consistent with the non-RRKM behavior found for the simulations of the O_3 + propene unimolecular dynamics.[124]

4.2.2. Thermal Unimolecular Kinetics. For a molecule consisting of s harmonic vibrational modes, it was found that the classical RRKM rate constant,

$$k(E) = \nu[(E - E_o)/E]^{s-1} \quad (3)$$

and classical TST rate constant,

$$k(T) = \nu \exp(-E_o/k_BT) \quad (4)$$

become equivalent for large E with $E_0/E \ll 1$, large $s \approx (s-1)$, and the energy and temperature of the of the s classical harmonic oscillators related by $E = sk_BT$.[135] This is seen by expressing the exponential in eq 4 as a power series. The conditions $E_0/E \ll 1$ and large $s \approx (s-1)$ are found for large molecules. For harmonic RRKM and TST theories, ν is the product of the molecular vibrational frequencies divided by the product of the TS vibrational frequenicies. An anharmonic correction may be included for ν. E_o is the classical barrier for the unimolecular reaction. Thus, a simulation of the unimolecular decomposition of a microcanonical ensemble for a large molecule, at energy E, may be used to determine the thermal unimolecular rate constant $k(T)$. This relationship is consistent with the understanding that, for a molecule with

DOI: 10.1021/jacs.6b12017
J. Am. Chem. Soc. 2017, 139, 3570−3590

large s and large E, the populations of the vibrational states of the individual oscillators are given by a Boltzmann distribution[13] and that the fluctuations of the energy of a grand canonical ensemble are negligible, making it similar to a microcanonical ensemble.[136] This relation between E and T has also been discussed with respect to product energies in unimolecular dissociation.[137]

The trajectories comprising this microcanonical ensemble are integrated until a unimolecular reaction occurs or up to a maximum time t_{max}. The total unimolecular rate constant k may be found by fitting the number of molecules remaining versus time:

$$N(t)/N(0) = \exp(-kt) \quad (5)$$

where $N(0)$ is the number of trajectories for the initial microcanonical ensemble at $t = 0$. If there are not a sufficient number of dissociations to accurately determine $N(t)/N(0)$, k may be approximated from the number of trajectories remaining at t_{max}:

$$N(t_{max})/N(0) = \exp(-kt_{max}) \quad (6)$$

The rate constant k, the total unimolecular rate constant $k(T)$, is the sum of the rate constants for the individual dissociation pathways $k(T) = \sum k_i(T)$. The individual $k_i(T)$ equal $k(T)$ multiplied by the number of dissociations for the ith pathway divided by the total number dissociations p_i; that is, $k_i(T) = p_i k(T)$. Plotting the logarithms of $k(T)$ and the $k_i(T)$ versus $1/T$ gives the Arrhenius parameters A and E_a for the overall reaction and the individual pathways. The above analysis assumes the unimolecular dissociation of the molecule is intrinsically RRKM so that a microcanonical ensemble is maintained during time as it dissociates. This can be tested by ensuring the unimolecular decay is exponential.

The classical Arrhenius activation energy E_a for unimolecular dissociation equals E_o, the difference between the classical potential energies of the dissociation TS and the unimolecular reactant, plus the difference between the average thermal energies of the TS and reactant.[138] The average classical thermal energy of the s vibrational modes of the reactant is sRT and for the $s - 1$ vibrational modes of the TS is $(s - 1)RT$. However, since the average thermal energy of the TS's reaction coordinate is RT, the average thermal energies of the TS and reactant are identical, and E_a is the same as E_o.[139]

In addition to providing Arrhenius parameters, the above simulation also identifies the molecule's unimolecular decomposition pathways at temperature T. The thermal unimolecular kinetics of the CH_3–NH–CH=CH–CH_3 molecule was studied by direct dynamics simulations at the MP2/6-31+G* level of theory for T = 3500–5500 K.[114,139] A total of 33 different primary decomposition pathways were observed.[114] The most predominant pathways are decomposition to form $^{\bullet}CH_3$ + $^{\bullet}$NH–CH=CH–CH_3 and isomerization to form CH_3–N=CH–CH_2–CH_3 and CH_3–NH–CH_2–CH=CH_2. The Arrhenius plot for forming the isomerization products is shown in Figure 7. The Arrhenius E_a from the simulations is 82.8 ± 4.3 and 64.9 ± 7.0 kcal/mol for the dissociation and isomerization pathways, respectively. The former is lower than the MP2/6-31+G* C–N dissociation energy of 87.8 kcal/mol and this is expected, since the C–N dissociation TS is variational and will have a potential energy less than the dissociation energy. For the isomerizations the stationary point TS potential energy is 62.8 kcal/mol and E_a from the simulations agrees with this value. The isomerization A-factor

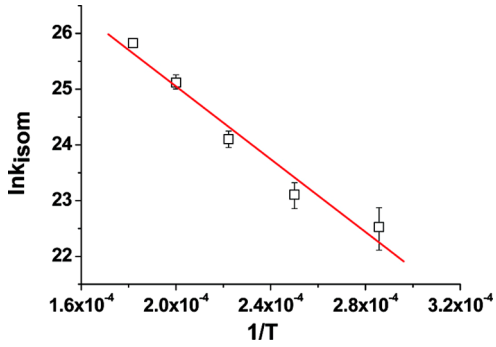

Figure 7. Plot of ln k_{isom} versus $1/T$ for forming the isomerization products CH_3–N=CH–CH_2–CH_3 and CH_3–NH--CH_2–CH=CH_2. The linear fit yields the Arrhenius parameters E_a = 64.9 ± 7.0 kcal/mol and $A = 5.2 + 4.5/-2.8 \times 10^{13}$ s^{-1}. The k_{isom} is in units of s^{-1}, and T is in K. Reproduced from ref 139 with permission from the American Chemical Society.

from the simulations is $5.2 + 4.5/-2.8 \times 10^{-13}$ s^{-1} and somewhat smaller than the TST value of 9.2×10^{-13} s^{-1} for the MP2/6-31+G* PES. This small difference may arise from anharmonic effects present in the simulations, but not in the harmonic TST calculations.

Direct dynamics simulations, utilizing the RM1 semiempirical electronic structure theory, were performed to study the thermal dissociation of the doubly protonated tripeptide threonine–isoleucine–lysine ion, TIK$(H^+)_2$, for temperatures of 1250–2500 K.[115] The number of different fragmentation pathways increases with increase in temperature. At 1250 K there are only four fragmentation pathways, with one contributing 85% of the fragmentation. In contrast, at 2500 K, there are 61 pathways, and not one dominates. A plot of the relative number of TIK$(H^+)_2$ ions versus time, $N(t)/N(0)$, is given in Figure 8a for the 1500 K simulations. The Arrhenius plot for the overall TIK$(H^+)_2$ dissociaton is given in Figure 8b. For four of the fragmentation pathways there were a sufficient number of dissociations at each temperature to determine their rate constants $k_i(T)$. Two of the pathways are homolytic C–C bond ruptures and their Arrhenius activation energies are consistent with the RM1 C–C bond dissociation energies. The two other pathways involve proton transfer, with stationary point TSs. The mechanism for one of the pathways is depicted in Figure 9 and its Arrhenius activation energy from the simulations is 14.7 ± 0.5 kcal/mol, in excellent agreement with RM1 TS energy of 15.0 kcal/mol. For the other proton transfer pathway the Arrhenius activation energy is 18.6 ± 0.5 kcal/mol, again in excellent agreement with RM1 TS energy of 18.3 kcal/mol.

4.3. Post-Transition-State Dynamics. The rate constant for a chemical reaction may be calculated from TST, if there is a rate-controlling TS, but for the *post-transition-state dynamics* it is necessary to understand the atomistic motion on the PES after passing the TS. The PES in this post-TS domain may have a very "rough" landscape, with multiple potential energy minima, reaction pathways, low energy barriers, etc., connecting the rate-controlling TS to multiple product channels. The important question is "what are the post-TS dynamics"? For example, do the trajectories follow the IRC,[32] which is the traditional model for the post-TS reaction path.[9]

A chemical dynamics simulation is an important method for studying post-TS dynamics. If TST is valid for a thermal unimolecular or bimolecular reaction, the chemical dynamics

DOI: 10.1021/jacs.6b12017
J. Am. Chem. Soc. 2017, 139, 3570–3590

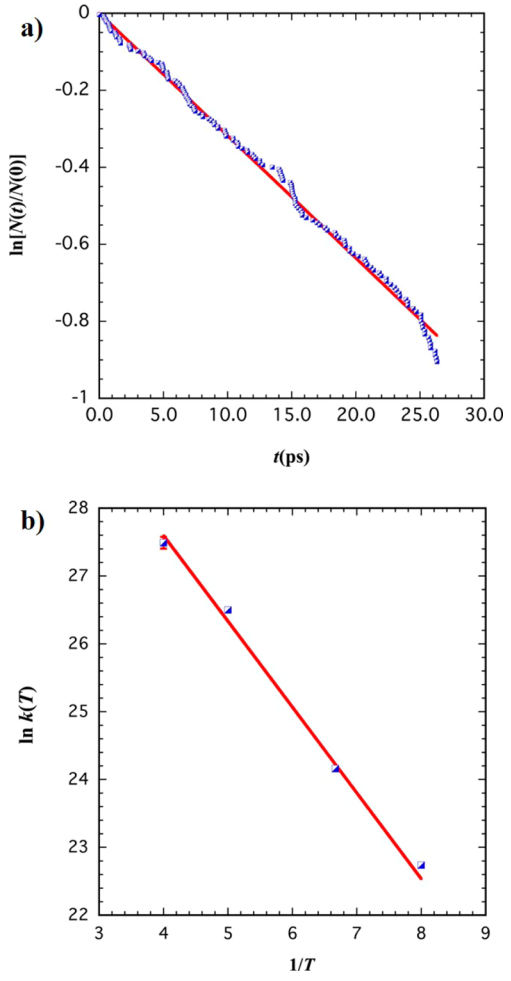

Figure 8. (a) Plot of $\ln[N(t)/N(0)]$ vs t for the 1500 K simulation of $TIK(H^+)_2$ dissociation. (b) Natural logarithm of the overall rate constant (s^{-1}) for $TIK(H^+)_2$ dissociation plotted vs 1/T (1×10^{-4} K^{-1}). The Arrhenius parameters are $A = (1.22 \pm 0.07) \times 10^{14}$ s^{-1} and $E_a = 24.2 \pm 0.2$ kcal/mol. Reproduced from ref 115 with permission from the American Chemical Society.

trajectories may be initiated at the TS for the reaction. For a fixed energy unimolecular reaction, which has statistical intramolecular dynamics, the trajectories may be initiated at the TS in accord with RRKM theory. For these simulations, canonical and microcanonical, the quasiclassical method which includes ZPE in the vibrational modes at the TS may be used to choose initial conditions for the trajectories. The dynamics in moving from the TS to products is usually a short-time event and a direct dynamics simulation, in which the PES for the reaction is directly represented by an electronic structure theory, is a computationally practical method for studying post-TS dynamics.

The important reaction dynamics properties which may be determined from post-TS dynamics simulations include (1) partitioning of the available energy to the products' relative translation, rotation, and vibration degrees of freedom; (2) branching between different product channels, which is particularly important for PES's with bifurcations in the exit-channel; (3) trapping in exit-channel potential energy minima and ensuing unimolecular dynamics, which is often non-statistical as described above; (4) possible avoidance of exit-channel minima in the multidimensional phase space for a chemical reaction; and (5) importance of TS recrossing. Properties (1), (2), (4), and (5) are illustrated by the following direct dynamics simulations.

4.3.1. Product Energy Partitioning and Reactant Reactive States. The dynamics in moving from the TS to products is of utmost importance in determining product energy partitioning. The dynamical attribute of interest is the manner in which the repulsive potential energy release in moving from the TS to products is partitioned between product relative translation, rotation, and vibration energies. These dynamics have been studied by direct dynamics for the $H_2CO \rightarrow H_2 + CO$ dissociation,[24,25,140] but a direct comparison with experiment is difficult since the roaming dissociation mechanism[141] was not included in the simulations. Here, post-TS product energy partitioning is illustrated by direct dynamics simulations for $C_2H_5F \rightarrow HF + C_2H_4$ dissociation,[142−144] and compared with experiments by Setser, Wittig, and co-workers,[145,146] in which the vibration and rotation energy distributions of the HF product were measured. The simulations were performed using MP2 theory with both the 6-31G* and 6-311++G** basis sets. The experimental 0 K potential energy release with ZPE included, E_r°, in going from the TS to products is 49.0 ± 2.0

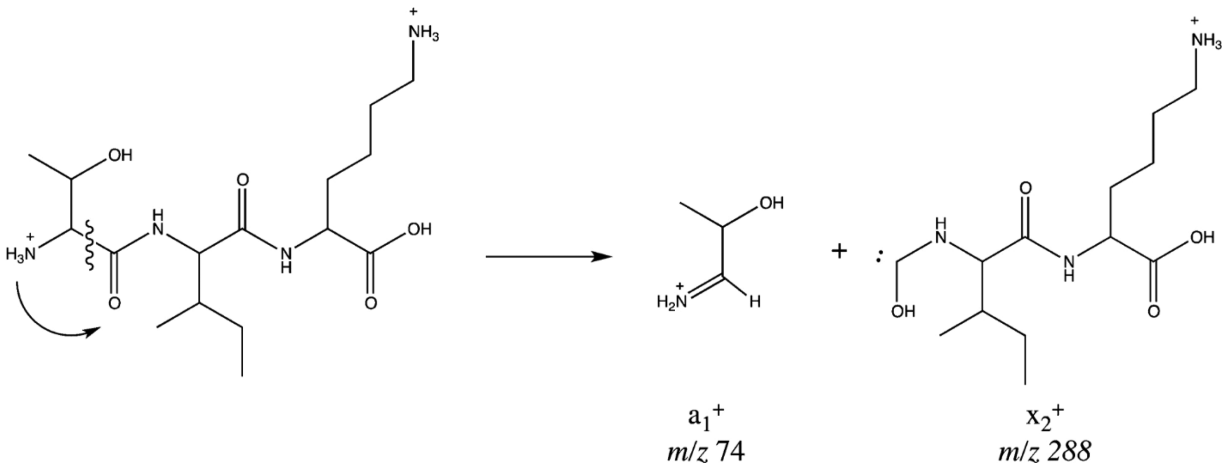

Figure 9. $TIK(H^+)_2$ dissociation mechanism for a proton transfer pathway. Reproduced from ref 115 with permission from the American Chemical Society.

DOI: 10.1021/jacs.6b12017
J. Am. Chem. Soc. 2017, 139, 3570−3590

kcal/mol, while the MP2 values with the 6-31G* and 6-311++G** basis sets are 45.3 and 50.6 kcal/mol, respectively.

An important comparison with experiment is the partitioning of the available product energy to HF vibration. For the experiments, excess energies at the TS ($E_{vt}^{\ddagger}$) of 32 and 42 kcal/mol were investigated. For the latter $E_{vt}^{\ddagger}$, the experiments show that 15% of the available energy is partitioned to HF vibration. The MP2/6-311++G** simulation gives 14% and nearly the same result, while the MP2/6-31G* simulation gives 8%. A more detailed comparison with experiment is the population distribution, $P(n)$, of the HF vibrational levels, which is shown in Figure 10. The MP2/6-311++G** simulations are in very good agreement with both the $E_{vt}^{\ddagger}$ = 32 and 42 kcal/mol experiments. Their principal difference is the small $P(1)/P(0)$ inversion found from the simulations.

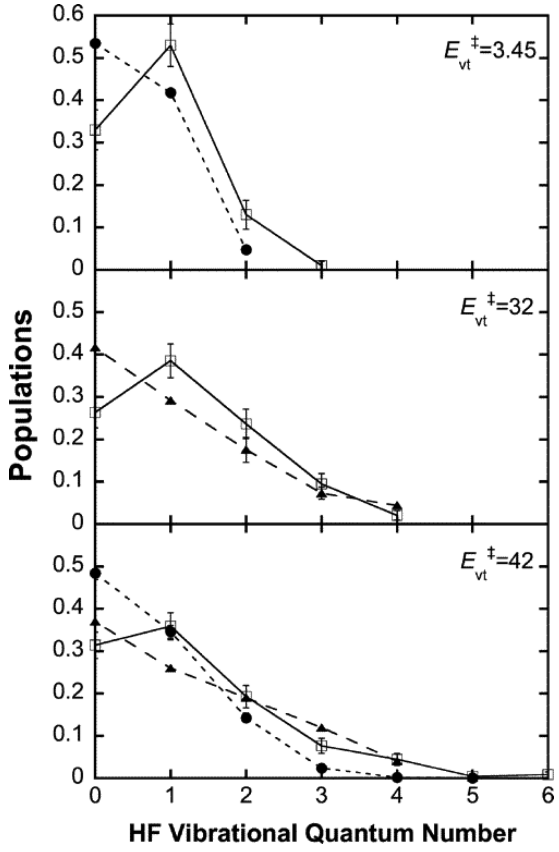

Figure 10. Populations of the HF vibrational states for $C_2H_5F \rightarrow HF + C_2H_4$ dissociation, with different amounts of vibration/reaction coordinate energy $E_{vt}^{\ddagger}$ in the $C_2H_5F^{\ddagger}$ transition state. □, results of the MP2/6-311++G** simulations; ●, results of the MP2/6-31G* simulations; and ▲, experimental results. The experimental results for $E_{vt}^{\ddagger}$ = 32 and 42 kcal/mol are from refs 146 and 145, respectively. Reproduced from ref 142 with permission from the American Institute of Physics.

Also of interest is the partitioning of the available energy to the products relative translation, rotation, and vibration degrees of freedom, obtained from the simulations but not the experiments. The results are given in Table 5. The majority of the product degrees of freedom are for C_2H_4 vibration and a statistical model would partition the majority of the product energy to C_2H_4 vibration. In contrast, as shown in Table 5, the majority of the energy is distributed to HF + C_2H_4 relative translation, arising from *nonstatistical, repulsive potential energy release* in moving from the TS to products. In comparing the results of the two basis sets, 6-311++G** partitions slightly less to relative translation and more to HF vibration, with the other energy partitionings similar for the two basis sets.

Following a model proposed by Zamir and Levine,[147] the product energy partitioning was analyzed versus $E_{vt}^{\ddagger}$ to determine the percentages of the potential energy release, E_r°, distributed to the different product energies. For the MP2/6-31G* simulations, the percentages partitioned to relative translation, C_2H_4 vibration, C_2H_4 rotation, HF vibration, and HF rotation are 81, 0, 5, 11, and 3%, respectively. For the MP2/6-311++G** simulations these percentages are 73, 2, 4, 18, and 3%. Thus, the vast majority of E_r° is partitioned to relative translation, with HF vibration coming in a distant second.

Xu et al. performed a B3LYP/6-31G* direct dynamics simulation,[148] similar to the direct dynamics for C_2H_5F dissociation,[149] except the trajectories were directed toward the reactants. Their simulation determined which reactant vibrational states have a high probability of attaining the TS structure and forming products for 1,3-dipolar addition reactions of diazonium betaines to acetylene and ethylene. The trajectories showed that reactant translation supplies the largest amount of energy needed to reach the TS, but reaction cannot proceed without a large amount of vibrational excitation in the bending mode of the betaine (i.e., N_2O, N_3H, and CH_2N_2).

4.3.2. Bifurcations and Branching between Exit-Channel Pathways. For a reaction whose PES has a bifurcation after passing the rate-controlling TS, chemical dynamics simulations are critical for predicting the product branching ratio.[150−155] A PES exhibiting a reaction path bifurcation is depicted in Figure 11. The intrinsic reaction coordinate (IRC)[32] leads to the valley−ridge inflection (VRI) point and then dynamics are needed to determine the branching between the two product channels. The branching will be determined by the dynamics in the vicinity of the VRI and these dynamics may be important either before or after the VRI.

Table 5. Average $C_2H_5F^{\ddagger} \rightarrow HF + C_2H_4$ Product Energy Partitioning for MP2/6-31G* and MP2/6-311++G Direct Dynamics[a]**

	MP2/6-31G*			MP2/6-311++G**		
product energy	$E_{vt}^{\ddagger}$ = 3.45	$E_{vt}^{\ddagger}$ = 27	$E_{vt}^{\ddagger}$ = 42	$E_{vt}^{\ddagger}$ = 3.45	$E_{vt}^{\ddagger}$ = 32	$E_{vt}^{\ddagger}$ = 42
rel trans	75.4	56.8	49.7	67.8(1.2)[b]	48.2(1.0)	46.2(1.0)
C_2H_4 vib	6.1	24.2	31.5	6.8(0.7)	26.2(0.8)	29.3(0.6)
C_2H_4 rot	4.6	5.9	6.0	5.1(0.3)	5.5(0.3)	6.2(0.3)
HF vib	10.5	8.7	7.9	16.9(1.3)	15.8(1.1)	14.0(1.0)
HF rot	3.4	4.4	4.9	3.4(0.3)	4.3(0.4)	4.3(0.3)

[a]The average energy partitioning is given in percentage. [b]The uncertainty, in parentheses, is the standard deviation of the mean.

DOI: 10.1021/jacs.6b12017
J. Am. Chem. Soc. 2017, 139, 3570−3590

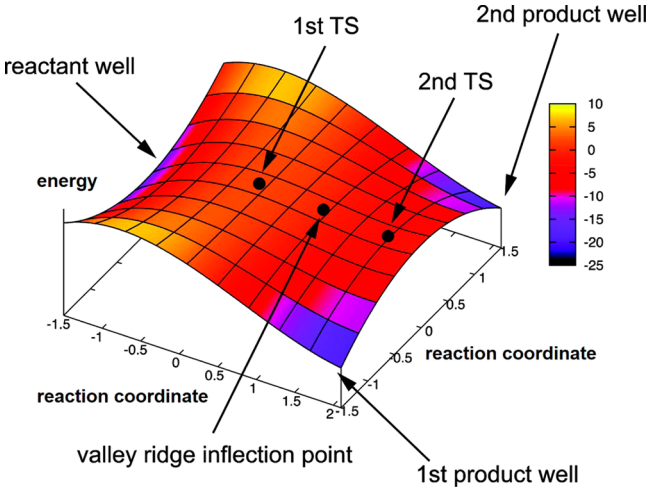

Figure 11. Model PES with a reaction path bifurcation and a valley–ridge inflection point. Reproduced from ref 152 with permission from the American Chemical Society.

A model PES has been developed to study nonstatistical dynamics associated with PESs with reaction path bifurcations and VRI points.[154] Simulations on this PES[154] indicate that, in the gas-phase, dynamics in the vicinity of the VRI are insignificant in determining the product branching, however for a reactive system with a strongly interacting solvent, and extensive energy transfer from the reactive system, the VRI may play an important role. Direct dynamics simulations are important for understanding the bifurcation dynamics for specific chemical reactions.[151,152,155−157] CASSCF(3,3)/6-31G* post-TS direct dynamics were used to study cyclopropyl radical ring opening.[156] For the IRC the CH_2 groups rotate disrotatroy, however the dynamics found that only 57% of the reaction followed the IRC and the remaining 43% followed a conrotatory path. In ensuing studies,[153,155] a reaction path bifurcation and a VRI were found to be important in interpreting the results of the direct dynamics simulations.

Enzymes may be important for *steering* natural product formation on PESs with reaction path bifurcations.[151,152] The biosynthesis of abietic acid involves a PES with a bifurcating reaction path.[151] This bifurcation is part of the C_{20} pimaradienyl cation rearrangement forming the abietadienyl cation, the natural product. A B3LYP/6-31+G** post-TS direct dynamics simulation was performed for a truncated C10 pimaradienyl cation to study its rearrangement.[151] Somewhat surprisingly a non-natural product was formed and the natural:non-natural product ratio was 1.6:1. Performing B3LYP simulations for the complete C20 pimaradienyl cation, but with the smaller 6-31+G* basis set, resulted in 1.3:1 for this ratio.[152] The simulations were performed in the absence of the enzyme and apparently it is needed to direct the reaction to only the natural product on the bifurcating PES.

The role of bifurcations in post-TS dynamics was studied by G96LYP/6-31G* direct dynamics for $[Ca(formamide)]^{2+}$ dissociation, for which Coulomb explosion and neutral loss unimolecular reactions compete.[157] The PES has bifurcations which give rise to non-IRC reaction dynamics. Non-IRC dynamics also arise from atomistic motions directing trajectories away from the IRC (see below). Different vibrational and rotational excitation patterns were considered for the for $[Ca(formamide)]^{2+}$ dissociation TSs and found to effect the branching between the Coulomb explosion and neutral loss pathways, the role of bifurcations on dissociation dynamics, and the importance of the different non-IRC mechanisms. Post-TS dynamics are quite important for this reaction.

4.3.3. Timing for Post-TS Bond Formation, Non-IRC Dynamics, and Avoiding Potential Energy Minima. Diels–Alder reactions between a diene and a dienophile involve two C−C bond formations. Post-TS direct dynamics simulations have been used to study the *timing* between these two bond formations for a series of Diels–Alder reactions.[158] At 298 K it was found that most of the reactions are essentially concerted, with a time gap between forming the two bonds which is shorter than a C−C vibrational period. At the higher temperature of ∼1000 K diradical character for the bond formation is observed in some of the trajectories. Simulating the Diels–Alder reaction in water increases the time gap between the two bond formations.[159]

The traditional model in moving from the TS toward products is that the reactive system follows the IRC.[9] If it leads to a potential energy minimum, RRKM theory is used to calculate the lifetime for trapping in the minimum and then the IRC is followed from the minimum to products. However, the IRC is an artificial, idealized trajectory with its kinetic energy removed after each infinitesimal step. For constant energy gas-phase reactions, trajectories usually do not follow the IRC. Above it was shown that, for PESs with reaction path bifurcations, the VRI point is usually unimportant and trajectories do not follow the IRC.

Non-IRC dynamics occur in direct dynamics simulations for reactions whose PESs do not have reaction path bifurcations. These dynamics were found for 1,2,6-heptatriene rearrangement,[122] the heterolysis rearrangement of protonated pinacolyl alcohol,[160] the $O(^3P) + CH_3 \rightarrow H_2 + H + CO$,[161] $F^- + CH_3OH$,[162] $OH^- + CH_3I$,[69] and $F^- + CH_3OOH$[163] reactions, and the microsolvated $OH^-(H_2O) + CH_3I$ and $F^-(H_2O) + CH_3I$ reactions.[106,109] The IRC often leads the reactive system to deep potential energy minima in the exit-channel, but in the multidimensional post-TS dynamics the non-IRC trajectories may avoid these minima. These dynamics are found in direct dynamics simulations for the $F^- + CH_3OH$, $OH^- + CH_3I$, $F^- + CH_3OOH$, $OH^-(H_2O) + CH_3I$, and $F^-(H_2O) + CH_3I$ reactions.[69,106,109,162,163] Non-IRC dynamics may also be important for the roaming reaction mechanism.[141]

To study post-TS dynamics for the $OH^- + CH_3F$ S_N2 reaction, MP2/6-31G* direct dynamics trajectories were initiated at the $[HO\text{--}CH_3\text{--}F]^-$ central barrier TS.[162] The IRC from the TS leads directly to an exit-channel potential energy minimum for the $CH_3OH\text{---}F^-$ intermediate. The trajectories do not follow this IRC and instead two different reaction pathways were found, one direct and the other indirect. The vast majority, ∼90%, follow a direct reaction pathway with departure of the F^- ion approximately along the O-C---F^- collinear axis and avoiding the potential energy minimum for the $CH_3OH\text{---}F^-$ intermediate. The remaining small fraction of trajectories initially follow the direct pathway, but they do not have sufficient $CH_3OH + F^-$ relative translational energy to dissociate and are drawn into the $CH_3OH\text{---}F^-$ minimum. As the system moves off the central barrier, it is propelled toward products by the potential energy release.

Similar dynamics are found for the $F^- + CH_3OOH$ reaction.[163] The potential energy curve for the $F^- + CH_3OOH$ reaction is shown in Figure 12. In experimental

DOI: 10.1021/jacs.6b12017
J. Am. Chem. Soc. 2017, 139, 3570−3590

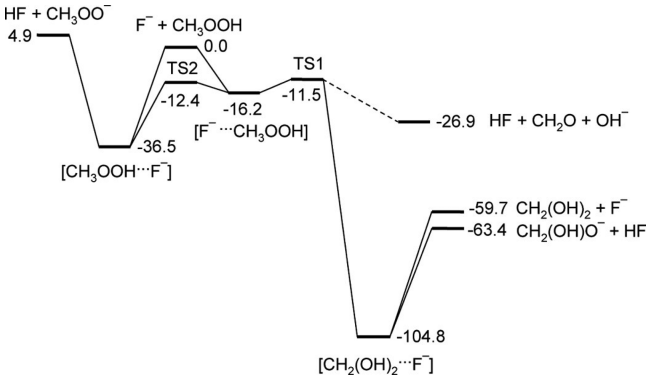

Figure 12. Energy diagram for the F^- + CH_3OOH reaction at the B3LYP/6-311+G** level of theory. The energies shown are in kcal/mol and are relative to the F^- + CH_3OOH reactant channel. Zero-point energies are not included. Reproduced from ref 163 with permission from the American Chemical Society.

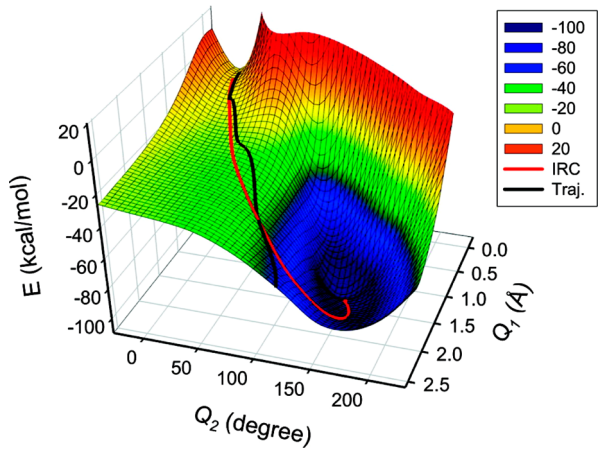

Figure 13. Two-dimensional contour diagram of the post-transition-state potential energy surface for TS1. $Q_1 = \Delta r_1 + \Delta r_2$, where r_1 is the FH−C bond length and r_2 is the O−OH bond length. $Q_2 = \Delta\theta_1 + \Delta\theta_2$, where $\Delta\theta_1$ is the O−C−O angle and $\Delta\theta_2$ is the H−O−C angle; i.e., H is the hydrogen abstracted by F^-, and O is the oxygen attached to carbon. Q_1 represents the concerted motion of HF and OH^- away from CH_2O, and Q_2 represents rotation of CH_2O. The remaining coordinates were optimized for each Q_1, Q_2 point. Depicted on this contour diagram is the IRC (red line) and a representative trajectory (black line). Reproduced from ref 163 with permission from the American Chemical Society.

studies of this reaction[164] it was found that the most exothermic products HF + $CH_2(OH)O^-$, and products predicted by the IRC are not formed. Instead, the much higher energy products HF + CH_2O + OH^-, formed by an $E_{CO}2$ mechanism, were observed. To provide an atomic-level understanding of these results, a B3LYP/6-311+G** direct dynamics simulation was performed with trajectories initiated for the F^- + CH_3OOH reactants. The post-TS dynamics for the trajectories, after passing TS1, did not follow the IRC to the deep potential energy minimum of the $CH_2(OH)_2$---F^- intermediate and instead directly formed the HF + CH_2O + OH^- products by the proposed $E_{CO}2$ mechanism. The branching between the HF + CH_2O + OH^- and HF + CH_3OO^- product channels found from the trajectories is in overall good agreement with the experimental estimate. The trajectory total reaction rate constant for F^- + CH_3OOH is in excellent agreement with the experimental value.

The non-IRC post-TS dynamics found for the F^- + CH_3OOH reaction is illustrated by the two-dimensional potential energy diagram in Figure 13.[163] Q_1 represents the concerted movement of HF and OH^- away from CH_2O, and Q_2 represents the in-plane rotation motion of CH_2O to access the deep potential energy minimum. Shown by the black line in Figure 13 is a representative trajectory, which "skirts" the deep potential energy minimum of $CH_2(OH)_2$---F^-. From the dynamics, the concerted movement of HF and OH^- away from CH_2O, is much faster than the rotation motion of CH_2O needed to access the potential energy minimum. Also, there is no barrier restricting the movement of HF and OH^- away from CH_2O. The red line illustrates the IRC leading to the complex. The dynamics for the F^- + CH_3OOH reaction are similar to those for the OH^- + CH_3F → CH_3OH + F^- reaction.

As found from direct dynamics simulation, deep exit-channel potential energy minima are also avoided for the microsolvated ions $OH^-(H_2O)$ and $F^-(H_2O)$ reacting with CH_3I.[106,109] The reaction dynamics are similar for these two ions and those for $OH^-(H_2O)$ are considered here. A schematic potential energy profile for the reaction is shown in Figure 5. The S_N2 reaction has a potential energy minimum for the CH_3OH---$I^-(H_2O)$ post-reaction complex. This complex was not formed in any of the trajectories. The dominant dynamics were for H_2O to dissociate from the system as $OH^-(H_2O)$ attached to CH_3I, with the associated potential energy release, or dissociate as OH^- displaced I^- with the much greater potential energy release. For $OH^-(H_2O)$ + CH_3I collision energies in the range of 2.0 to 0.05 eV, the $I^-(H_2O)/I^-$ ratio varies from 0.011 to 0.021 from the experiments and 0.018 to 0.041 from the simulations.

4.3.4. TS Recrossing. TST assumes that a trajectory that crosses the TS in the direction reactants → products does not recross the TS.[138] If there are recrossings the TST rate constant is corrected by the recrossing factor κ; i.e., $k = \kappa k_{TST}$. Central barrier recrossing is important for the Cl^- + CH_3Cl S_N2 reactions.[165,166] MP2/6-31G* direct dynamics trajectories were initiated at the $[Cl\text{--}CH_3\text{--}Cl]^-$ central barrier with a 300 K Boltzmann distribution of energy as assumed by TST and then integrated in both the reverse and forward directions for 3 ps.[166] Substantially recrossing was observed, with trajectories trapped in the vicinity of the central barrier, yielding a κ factor of 0.2. A smaller κ factor is expected if the trajectories were integrated for a longer period of time, giving rise to more recrossings. A similar study using an analytic PES gave κ = 0.1 for trajectories integrated for 40 ps.[165]

Central barrier recrossing are much less important for the Cl^- + CD_3Cl and Cl^- + C_2H_5Cl S_N2 reactions.[167,168] For trajectories initiated at the $[Cl\text{---}CD_3\text{---}Cl]^-$ central barrier, and integrated in both the forward and reverse directions for 3 ps, κ = 0.7 as compared to 0.2 for Cl^- + CH_3Cl.[166] This difference may result from the lower intramolecular vibrational frequencies for CD_3Cl as compared to CH_3Cl, giving rise to more couplings between the low and high frequency vibrational modes of the reactive system and less phase space trapping in the vicinity of the central barrier. For the Cl^- + C_2H_5Cl S_N2 reaction, there is negligible recrossing of the central barrier.[168] There is substantial IVR between the reactive system's low and high frequency vibrational modes.

Central barrier recrossing was also found to be important in a direct dynamics simulation of the F^- + NH_2F S_N2 reaction.[169]

4.4. Mass Spectrometry Simulations. *4.4.1. Surface-Induced Dissociation (SID) Energy Transfer and Fragmenta-*

DOI: 10.1021/jacs.6b12017
J. Am. Chem. Soc. 2017, 139, 3570−3590

Table 6. QM+MM Dynamics for Peptide-H^+ Ions Colliding with a Diamond {111} Surface

ion	V_{ion}	θ_i	E_i (eV)	% shattering	pathways	$\langle \Delta E_{int} \rangle$[a]	ref
gly-H^+	AM1	45°	70	23	18	12	172
gly-H^+	MP2	0°	70	57	96	17	173
		45°	70	22	14	11	
gly_2-H^+	AM1	0°	30	8	6	24	112
		0°	50	13	23	21	
		0°	70	44	44	20	
		45°	70			12	
		0°	100	71	59	17	
gly_8-H^+	AM1	0°	100	78	304	45	113
		45°	100	22	*b*	26	

[a]Average percentage energy transfer to vibration and rotation of the peptide ion. [b]Not determined.

tion Dynamics. Direct dynamics simulations have greatly assisted in establishing atomistic understandings of the dynamics associated with collisions of protonated peptide ions, peptide-H^+, with organic surfaces.[170,171] Two types of direct dynamics models were used for the simulations. For one, identified as QM+MM, the potential for peptide-H^+, $V_{peptide}$, is represented by a quantum mechanical (QM) theory, while the surface and peptide−surface potentials, i.e., $V_{surface}$ and $V_{peptide\text{-}surface}$, are represented by molecular mechanical (MM) functions. For the other, called QM/MM, reaction is allowed between peptide-H^+ and the surface by including part of the surface in the QM calculation. The remaining part of the surface and its interaction with peptide-H^+ is MM. The organic surfaces considered in the simulations are diamond {111}, and alkylthiolate and perfluorinated alkylthiolate self-assembled monolayers, i.e., H-SAM and F-SAM, and the peptide-H^+ ions are polyglycines, gly_n-H^+.

A critical component of peptide-H^+ ion SID is the efficiency of transfer of the ion's collision energy E_i to the ion's vibrational modes so that it can fragment. The energy transfer efficiencies for collision with the diamond {111} surface are summarized in Table 6.[112,113,172,173] Energy transfer dynamics for the AM1 and MP2 QM models were compared for gly-H^+ + diamond collisions for an incident collision angle θ_i = 45° (θ_i = 0° is normal to the surface) and collision energy E_i = 70 eV. The AM1 and MP2 average percentage energy transfers to peptide-H^+ internal energy, the surface, and final peptide-H^+ translation energy are the same and are respectively 12, 38, and 50%. The AMBER MM model for $V_{peptide}$ gives statistically the same energy transfer percentages,[172,174] which indicates that the much more computationally efficient AMBER model may be used to obtain accurate energy transfer dynamics for peptide-H^+ + surface collisions.

Consistent with experiment,[175,176] the percentage of energy transfer to the peptide ion's internal energy is only weakly dependent on the collision energy for collisions with both the diamond and H-SAM surfaces. These dynamics are illustrated by AM1 simulations of gly_2-H^+ + diamond {111} collisions at θ_i = 0° (Table 6) and PM3 and RM1 simulations of gly_8-H^+ + H-SAM collisions.[177] In contrast, energy transfer to the surface and to peptide-H^+ final translational energy increase and decrease, respectively, with increase in E_i. For collisions with the H-SAM surface, energy transfer to peptide-H^+ internal energy is insensitive to the incident angle. This may result from the high corrugation and substantial roughness of the H-SAM surface. Contrary to the insensitivity of this energy transfer on θ_i, energy transfer to the surface and that remaining in peptide-H^+ translation decrease and increase, respectively, as θ_i is increased from 0 to 45°. The dependence of energy transfer on θ_i is different for peptide-H^+ collisions with diamond {111}. As shown in Table 6, there is a decrease in transfer to peptide-H^+ internal energy upon changing θ_i from 0 to 45°.This decrease in energy transfer is approximately the same as that expected for $\cos^2 \theta_i$ scaling, which equals 0.5. The dependence of energy transfer to the surface and remaining in translation, on θ_i, is the same as that above for the H-SAM.

In experiments of peptide-H^+ collisions with SAM surfaces,[175,176] the percentage transfer to the peptide ion's internal energy is only weakly dependent on the ion's size. This is found from PM3 and RM1 simulations with the H-SAM and θ_i = 45°, for which the percentage energy transfer to peptide-H^+ internal energy is 7−8% for gly_3-H^+ and 10−14% for gly_8-H^+.[177,178] In contrast as shown in Table 6, for collisions with diamond {111} energy transfer to peptide-H^+ internal energy does depend on the ion's size.

Two mechanisms were found for fragmentation of the peptide-H^+ ions.[112,113,172,173] For the traditional energy transfer mechanism, peptide-H^+ is vibrationally excited by its collision with the surface, rebounds off the surface, and then dissociates after IVR. The simulations revealed an unforeseen type of fragmentation, called shattering, in which peptide-H^+ fragments as it collides with the surface and is the origin of the large increase in number of product channels observed experimentally with increase in collision energy.[179,180] Collisions of peptide-H^+ with the surface directly drive the peptide ion to dissociation TSs, so that it dissociates nonstatistically as it collides with the surface. For QM+MM direct dynamics simulations of collisions of gly_n-H^+, n = 1, 2, and 8, colliding with the diamond {111} surface, the shattering percentages are given in Table 6. For the gly_2-H^+ collisions with θ_i = 0°, shattering increases from 8 to 71% as E_i is increased from 30 to 100 eV, an increase consistent with experiment. For the gly-H^+ collision, AM1 and MP2 with θ_i = 45° and E_i = 70 eV give nearly identical shattering percentages.

Concomitant with the increase in shattering, as E_i is increased, is the dramatic increase in the number of fragmentation pathways, the signature of shattering in the experiments. For gly_2-H^+ the number of fragmentation pathways increases from 6 to 59 as E_i is increased from 30 to 100 eV for normal θ_i = 0° collisions. For collisions of the large

DOI: 10.1021/jacs.6b12017
J. Am. Chem. Soc. 2017, 139, 3570−3590

peptide ion gly_8-H^+ at 100 eV, there are 304 different fragmentation pathways! Many are related by their backbone cleavage patterns. The MP2 simulations for gly-H^+, and those for gly_8-H^+ with AM1, show there is a marked decrease in the shattering percentage and the number of dissociation pathways as θ_i is changed from a normal 0° collision to 45°. Importantly, for the gly-H^+ simulations at 45°, MP2 and AM1 give very similar results for the percentage shattering and the number of dissociation pathways. For the same E_i and θ_i, the shattering percentage is not strongly dependent on the size of peptide-H^+. Shattering is also important in QM/MM simulations, with RM1, for gly_2-H^+ collisions at $\theta_i = 0°$ with −COCl and −CHO terminally terminated F-SAM surfaces.[181] Shattering is not important for gly_2-H^+ and gly_8-H^+ collisions with the softer H-SAM surface, as found from PM3 and RM1 simulations.[177,182]

4.4.2. Proton Migration and Conformational Dynamics for Peptide-H^+. The mobile proton model, proposed by Wysocki and co-workers,[183,184] provides a qualitative framework in which to consider long-time fragmentation events. Within this model, energy transfer allows proton migration from lower energy to higher energy sites, which in turn leads to backbone cleavage. Direct dynamics studies of SID have captured the mobile proton model in action.[185−187] These works have shown that proton motion is well correlated with peptide fragmentation and in fact the lag time between proton transfer and bond cleavage found from simulations is well described using a simple three state kinetic model.[185] It was found that 90% of fragmentation events that are attributed to proton motion occur within 1.5 ps of the relevant proton migration at a collision energy of 110 eV and within 2.5 ps at the lower collision energy of 30 eV. The first proton transfer is found to be the most likely to induce fragmentation with an efficiency for fragmentation at ∼50%, with the proton typically moving to the closest available protonation site. Different conformational families exhibited different proton transfer pathways, and hence different fragmentation products.[187] This is a striking result as one might have expected the collision event to cause a loss of memory of the initial conformation.

4.4.3. Fragment Complexations. A quite interesting finding from the SID simulations, is the post-fragmentation dynamics. Following the initial collision event and fragmentation, it is possible for the peptide fragments to form non-covalent complexes with the charged fragment hydrogen bonding to various protonation sites along the neutral fragment.[186] These complexes may have a relatively long lifetime. For collisions of gly_8-H^+ with the F-SAM surface, complexes formed between $(NH_2CH_2)^+$ and gly_7 have average lifetimes of 5.7 and 4.3 ps at a collision energy of 30 and 110 eV, respectively. This is an important finding given that this is a sufficiently long period of time for the excess proton to transfer between peptide fragments. Proton transfer via complexation allows for new proton transfer pathways that may not have been otherwise considered. These complexations lead to fragmentations in which the atoms of the peptide backbone are rearranged. This class of proton transfer works in concert with the "traditional" proton migration mechanism and certain products can only be obtained with both processes occurring within the same secondary fragmentation event.

4.4.4. Reactive Landing. Reactive landing is found to follow a four-centered TS in RM1 QM/MM simulations of gly_2-H^+ colliding with both an F-SAM[181] and an H-SAM.[182] A TS that involves four bodies is rather unusual and is deserving of some additional explanation. In the four-centered TS, two bonds break, while two new bonds form. Namely, the bonds that break are typically an X−H bond of the peptide along with the C−G bond of the surface, where X is a heavy atom of the peptide backbone, and G is the "leaving group" of the modified headgroup. The bonds that form are G−H and C−X. For the simulations with both the F-SAM and H-SAM surfaces, intact surface deposition was found and compared favorably with the experimental work of Laskin and co-workers.[188] Reactivity between the peptide and the surface was found to monotonically increase with collision energy. It was only when the specific subclass of intact surface deposition was considered that the characteristic peak in reactive landing observed in experiment was also seen in the simulations. As the collision energy increases, reactivity certainly does increase, however, the probability for the modified headgroup breaking off of the surface also increases. It was also found that the F-SAM had a significantly higher reactivity than the H-SAM, which was attributed to the relative stiffness of the two surfaces and how a stiff surface tends to hold two of the four atoms relatively in-place during the collision, while they are relatively free to move away in the floppy H-SAM.[182]

4.4.5. Collision-Induced Dissociation (CID). Direct dynamics simulations have played an important role in identifying important dynamical attributes of CID of organic and biological molecules.[115,172,189−201] The experiments involve collisions with an inert gas such as N_2 or a rare gas versus the collision energy, and the simulations are important for comparing with and interpreting the experiments. The simulations provide essential information regarding (1) the fundamental dynamics for the unimolecular dissociation of the organic and biological molecules; (2) the vibrational and rotational energy distributions of the excited molecules; (3) the ions formed by the CID process, which may be directly compared with experiment; and (4) mechanism for the CID fragmentation.

The simulations show that the CID unimolecular dissociation consists of two mechanisms. A shattering mechanism, similar to that described above for SID, in which dissociation occurs during the collision, and the traditional, statistical, RRKM mechanism, with efficient IVR. The CID dissociation may be described by a composite of these two mechanisms.[194] Critical for the RRKM component of the modeling are the vibrational and rotational energy distributions of the excited molecule. For some molecules the rotational excitation is as large as the vibrational.[189,191] For some of the simulations, like that for testosterone CID,[200] the ion fragments and their intensities are in quite good agreement with experiment.

Important, and revealing from the simulations, is the elucidation of the fragmentation pathways. Pathways for the statistical, RRKM calculations may be determined by stationary point calculations of TS structures and energies, and these properties for reaction intermediates and products. However, the nonstatistical, shattering pathways are often unexpected and only revealed by the direct dynamics simulations. The CID pathways found from the simulations for protonated Gly_2NH_2 and Gly_3NH_2 are in quite good agreement with the ions found experimentally.[195] Fragmentation mechanism determined for protonated uracil from simulations are consistent with those deduced from isotopic labeling experiments.[196] Another strength from the simulations is that they identify the neutral products, which are not observed in the mass spectrometry experiments. The simulations also confirm proposed mechanistic models, such as the mobile proton model for peptide ion fragmentation.[115,192,195,197]

DOI: 10.1021/jacs.6b12017
J. Am. Chem. Soc. 2017, 139, 3570−3590

4.5. Semiclassical (SC) Anharmonic Vibrational Spectra. Direct dynamics methods may be implemented in SC chemical dynamics,[90,202] in which all quantum effects are included in the classical mechanics.[203,204] The semiclassical initial value representation (SC-IVR) theory has been developed as a powerful and accurate tool for calculating anharmonic molecular vibrational spectral densities, which exclusively relies on classical trajectories. It is straightforward to implement a SC-IVR direct dynamics simulation. The vibrational spectrum power spectrum density in the time-averaging (TA) SC-IVR approach, using the Heller−Herman−Kluk−Kay (HHKK) semiclassical propagator approximation[204−206] with the separable approximation,[207] is given by

$$I(E) = \frac{(2\pi\hbar)^{-F}}{2\pi\hbar T}\int \mathrm{d}p(0)\int \mathrm{d}q(0)\times \left|\int_0^T \mathrm{d}t\langle\chi|p(t)q(t)\rangle\, \mathrm{e}^{i\{S_t[p(0),q(0)]+Et+\phi_t[p(0),q(0)]\}/\hbar}\right|^2 \quad (7)$$

where the sets of $(p(t),q(t))$ are the momenta and position variables propagated from the initial phase space point $(p(t),q(0))$, and the reference state $|\chi\rangle$ may be chosen as a combination of multiple coherent states (MC),[208,209] i.e.,

$$|\chi\rangle = \sum_{i=1}^{N_{\text{states}}} |p_{\text{eq}}^i, q_{\text{eq}}^i\rangle \quad (8)$$

to give the MC-SC-IVR implementation of the semiclassical theory.

In theory, what makes direct SC-IVR dynamics computationally impractical is the need to (1) calculate a large ensemble of trajectories for proper averaging and (2) calculate the Hessian at each integration step. However, in practice both of these are unnecessary. With time averaging and more importantly the MC-SC-IVR method,[208−210] eq 7 may be solved with only a small number of trajectories. In addition, with the compact finite difference (CFD) algorithm described above,[89] it is unnecessary to calculate the Hessian from electronic structure theory at each integration step.

The results of MC-SC-IVR simulations of the CO_2 anharmonic spectrum are given in Figure 14.[203] The direct dynamics are performed at the B3LYP/cc-pVDZ level of theory. Using the MC method only eight trajectories were calculated for the simulation. Spectra are given in Figure 14 for different values of K, which is the number of Hessian updates before calculating the Hessian from electronic structure theory. Only at K = 70 does the power spectrum begin to have peaks missing and deviations on the order of 10 cm^{-1}. Using the CFD interpolation, the computation time is reduced by 2 orders of magnitude at K = 70 using a velocity Verlet algorithm.

4.6. Electronic Non-adiabatic Direct Dynamics. Electronic non-adiabatic processes are often accurately described by direct dynamics simulations,[211,212] and such studies have been particularly helpful for understanding the photodynamics of biological molecules, e.g., nucleobases,[213] and interpreting experiments. These simulations are performed using PESs for multiple electronic states (e.g., S_0, S_1, and S_2), with the trajectory undergoing transitions between the PESs. For each numerical integration time step, the trajectory motion is calculated for a single PES, but non-adiabatic couplings are used to calculate the probability for a transition to a different PES. The trajectory surface-hopping algorithm[211,212] or the *ab initio* multiple spawning method[214] may be used to determine the transition probabilities between the PESs. These electronic non-adiabatic transitions are pronounced at conical intersections (see Figure 15).[214,215]

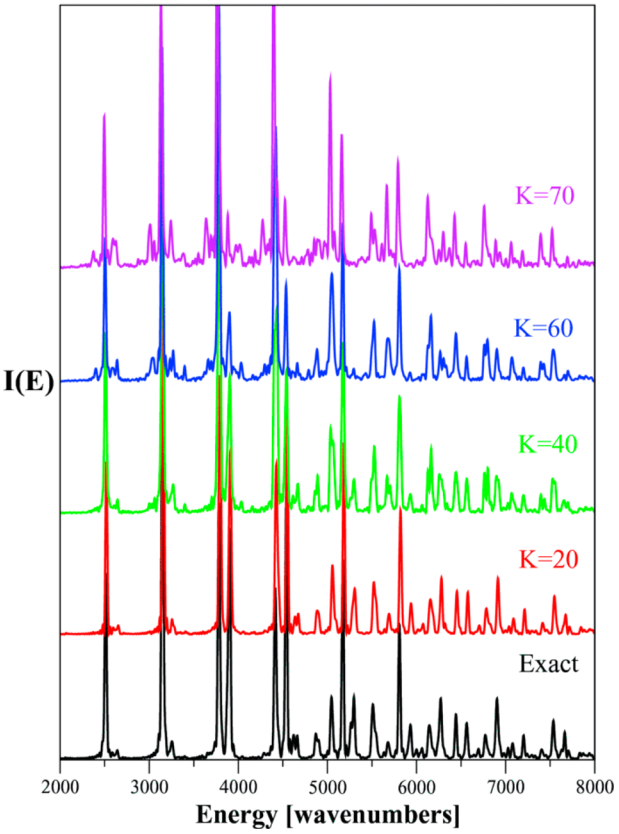

Figure 14. Direct dynamics power spectra for carbon dioxide calculated at different levels of the CFD-Bofill Hessian update scheme and B3LYP/cc-pVDZ theory. The simulations were performed with the MC-SC-IVR method using eight trajectories. The black line is the spectrum without the Hessian CFD approximation and the colored lines are for different levels of the CFD Hessian approximation. Reproduced from ref 203 with permission from the American Institute of Physics.

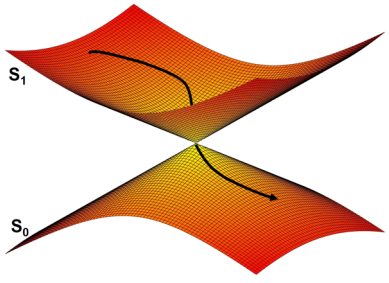

Figure 15. Illustration of a canonical intersection between two PESs.

Findings from these electronic non-adiabatic direct dynamics simulations, of biological molecules, are profound. The simulations show that UV-photoexcited DNA and RNA nucleobases are structurally stable as a result of a rapid $S_1 \rightarrow S_0$ internal conversion at a conical intersection, converting the electronic excitation into heat.[213] Similar dynamics are found for retinal models[216,217] and 9*H*-adenine,[218] and for the UV-filtering capacity of kynurenines.[219] The simulations have also illustrated that hydrogen bonding has a pronounced effect on

DOI: 10.1021/jacs.6b12017
J. Am. Chem. Soc. 2017, 139, 3570−3590

the electronic non-adiabatic dynamics of adenine in DNA strands[220] and of the GFP chromophore.[221,222]

5. THE FUTURE

In the future, direct dynamics simulations are expected to play an even more important role in modeling chemical and biochemical reactions. Above, direct dynamics simulations are described for bimolecular S_N2 nucleophilic substitution, unimolecular decomposition with both random and non-random vibrational excitation, nonstatistical chemical dynamics for organic and bioorganic reactions, non-IRC reaction dynamics, mass spectrometry fragmentation dynamics, and semiclassical calculation of anharmonic vibrational spectra. Direct dynamics allows one to study a broad range of chemical and biochemical problems, and the study of even a broader range of problems with more complexity is expected in the future.

Direct dynamics involves the coupling between chemical dynamics and electronic structure theory. Enhancements in the computational efficiency of direct dynamics are important and they may come from either or both of these two domains. It is important to have efficient, but still accurate electronic structure methods, and recent work in developing more accurate DFT functionals[223,224] is quite important in this regard. The simulations will also be enhanced by developing more efficient algorithms for integrating the classical equations of motion, for which some work has been done.[83−89] The next step forward seems to be the need to accurately interpolate the PES information acquired during the direct dynamics simulation, to avoid as many costly electronic structure calculations as possible. The most efficient way to do this may be to perform the simulations in parallel so that information between all the trajectories may be shared. Thus, efficient parallelization of the direct dynamics simulations may be important. The future for direct dynamics simulations is exciting for the broad range of possible applications and the possibilities for enhancing the simulations.

AUTHOR INFORMATION

Corresponding Author

*bill.hase@ttu.edu

Notes

The authors declare no competing financial interest.

ACKNOWLEDGMENTS

The direct dynamics simulations by the Hase research group are supported by the National Science Foundation under Grant No. CHE-1416428, the Robert A. Welch Foundation under Grant No. D-0005, and the Air Force Office of Scientific Research under AFOSR Award Nos. FA9550-16-1-0133 and FA9550-17-1-0119. The authors wish to thank Dr. Jing Xie for helpful comments.

REFERENCES

(1) Truhlar, D. G.; Muckermann, J. T. In *Atom-Molecule Collision Theory*; Bernstein, R. B., Ed.; Plenum: New York, 1979; pp 505−566.
(2) Peslherbe, G. H.; Wang, H.; Hase, W. L. *Adv. Chem. Phys.* **1999**, *105*, 171−202.
(3) Bunker, D. L. *J. Chem. Phys.* **1962**, *37*, 393−403.
(4) Bunker, D. L. *J. Chem. Phys.* **1964**, *40*, 1946−1957.
(5) Blais, N. C.; Bunker, D. L. *J. Chem. Phys.* **1962**, *37*, 2713−2720.
(6) Karplus, M.; Porter, R. N.; Sharma, R. D. *J. Chem. Phys.* **1965**, *43*, 3259−3287.
(7) Bosio, S. B. M.; Hase, W. L. *J. Chem. Phys.* **1997**, *107*, 9677−9686.
(8) Troya, D.; Schatz, G. C. *J. Chem. Phys.* **2004**, *120*, 7696−7707.
(9) Lourderaj, U.; Park, K.; Hase, W. L. *Int. Rev. Phys. Chem.* **2008**, *27*, 361−403.
(10) Lu, D.-h.; Hase, W. L. *J. Phys. Chem.* **1988**, *92*, 3217−3225.
(11) Zhang, Y.; Barnes, G. L.; Yan, T.; Hase, W. L. *Phys. Chem. Chem. Phys.* **2010**, *12*, 4435−4445.
(12) Chapman, S.; Bunker, D. L. *J. Chem. Phys.* **1975**, *62*, 2890−2899.
(13) Park, K.; Engelkemier, J.; Persico, M.; Manikandan, P.; Hase, W. L. *J. Phys. Chem. A* **2011**, *115*, 6603−6609.
(14) Hirst, D. M. *Potential Energy Surfaces*; Taylor and Francis: London, 1985.
(15) Hase, W. L.; Mrowka, G.; Brudzynski, R. J.; Sloane, C. S. *J. Chem. Phys.* **1978**, *69*, 3548−3562.
(16) Braams, B. J.; Bowman, J. M. *Int. Rev. Phys. Chem.* **2009**, *28*, 577−606.
(17) Bowman, J. M.; Czakó, G.; Fu, B. *Phys. Chem. Chem. Phys.* **2011**, *13*, 8094−8111.
(18) Bolton, L.; Hase, W. L.; Peslherbe, G. H. In *Modern Methods for Multidimensional Dynamics Computations in Chemistry*; Thompson, D. L., Ed.; World Scientific: London, 1998; pp 143−189.
(19) Sun, L.; Hase, W. L. *Rev. Comput. Chem.* **2003**, *19*, 79−146.
(20) Wang, I. S. Y.; Karplus, M. *J. Am. Chem. Soc.* **1973**, *95*, 8160−8164.
(21) Leforestier, C. *J. Chem. Phys.* **1978**, *68*, 4406−4410.
(22) Helgaker, T.; Uggerud, E.; Jensen, H. J. A. *Chem. Phys. Lett.* **1990**, *173*, 145−150.
(23) Uggerud, E.; Helgaker, T. *J. Am. Chem. Soc.* **1992**, *114*, 4265−4268.
(24) Chen, W.; Hase, W. L.; Schlegel, H. B. *Chem. Phys. Lett.* **1994**, *228*, 436−442.
(25) Peslherbe, G. H.; Hase, W. L. *J. Chem. Phys.* **1996**, *104*, 7882−7894.
(26) Peslherbe, G. H.; Wang, H.; Hase, W. L. *J. Am. Chem. Soc.* **1996**, *118*, 2257−2266.
(27) Doubleday, C., Jr.; Bolton, K.; Peslherbe, G. H.; Hase, W. *J. Am. Chem. Soc.* **1996**, *118*, 9922−9931.
(28) Warshel, A.; Levitt, M. *J. Mol. Biol.* **1976**, *103*, 227−249.
(29) Benedek, R.; Alavi, A.; Seidman, D. N.; Yang, L. H.; Muller, D. A.; Woodward, C. *Phys. Rev. Lett.* **2000**, *84*, 3362−3365.
(30) Barnett, R. N.; Landman, U. *Phys. Rev. B: Condens. Matter Mater. Phys.* **1993**, *48*, 2081−2097.
(31) Janke, S. M.; Auerbach, D. J.; Wodtke, A. M.; Kandratsenka, A. *J. Chem. Phys.* **2015**, *143*, 124708.
(32) Fukui, K. *J. Phys. Chem.* **1970**, *74*, 4161−4163.
(33) Gonzalez-Lafont, A.; Truong, T. N.; Truhlar, D. G. *J. Phys. Chem.* **1991**, *95*, 4618−4627.
(34) Car, R.; Parrinello, M. *Phys. Rev. Lett.* **1985**, *55*, 2471−2474.
(35) Štich, I.; Car, R.; Parrinello, M. *Phys. Rev. B: Condens. Matter Mater. Phys.* **1991**, *44*, 11092−11104.
(36) Allen, M. P.; Tildesley, D. J. *Computer Simulations of Liquids*; Clarendon: Oxford, 1996.
(37) Hase, W. L., Ed. *Comparisons of Classical and Quantum Dynamics*; Jai Press: London, 1998.
(38) Schatz, G. C. In *Comparisons of Classical and Quantum Dynamics*; Hase, W. L., Ed.; Jai Press: London, 1998; pp 205−230.
(39) Lu, D.-h.; Hase, W. L. *J. Chem. Phys.* **1988**, *89*, 6723−6735.
(40) Miller, W. H.; Hase, W. L.; Darling, C. L. *J. Chem. Phys.* **1989**, *91*, 2863−2868.
(41) Bunker, D. L.; Hase, W. L. *J. Chem. Phys.* **1973**, *59*, 4621−4632.
(42) Hase, W. L.; Buckowski, D. G. *J. Comput. Chem.* **1982**, *3*, 335−343.
(43) Swamy, K. N.; Hase, W. L. *J. Phys. Chem.* **1983**, *87*, 4715−4720.
(44) Skodje, R. T.; Truhlar, D. G.; Garrett, B. C. *J. Phys. Chem.* **1981**, *85*, 3019−3023.
(45) Dobbyn, A. J.; Stumpf, M.; Keller, H.-M.; Schinke, R. *J. Chem. Phys.* **1996**, *104*, 8357−8381.

DOI: 10.1021/jacs.6b12017
J. Am. Chem. Soc. 2017, 139, 3570−3590

(46) Pollak, E.; Child, M. S. *Chem. Phys.* **1981**, *60*, 23−32.
(47) Pollak, E. *Comments At. Mol. Phys.* **1984**, *15*, 73−85.
(48) Dong, W.; Xiao, C.; Wang, T.; Dai, D.; Yang, X.; Zhang, D. H. *Science* **2010**, *327*, 1501−1502.
(49) Wang, T.; Chen, J.; Yang, T.; Xiao, C.; Sun, Z.; Huang, L.; Dai, D.; Yang, X.; Zhang, D. H. *Science* **2013**, *342*, 1499−1502.
(50) Yang, T.; Chen, J.; Huang, L.; Wang, T.; Xiao, C.; Sun, Z.; Dai, D.; Yang, X.; Zhang, D. H. *Science* **2015**, *347*, 60−63.
(51) Miller, R. E.; Vohralik, P. F.; Watts, R. O. *J. Chem. Phys.* **1984**, *80*, 5453−5457.
(52) Tobiason, J. D.; Dunlop, J. R.; Rohlfing, E. A. *J. Chem. Phys.* **1995**, *103*, 1448−1469.
(53) Stumpf, M.; Dobbyn, A. J.; Mordaunt, D. H.; Keller, H.-M.; Fluethmann, H.; Schinke, R.; Werner, H.-J.; Yamashita, K. *Faraday Discuss.* **1995**, *102*, 193−213.
(54) Pollak, E. *J. Chem. Phys.* **1982**, *76*, 5843−5848.
(55) Paul, A. K.; Kolakkandy, S.; Pratihar, S.; Hase, W. L. In *Reaction Rate Constant Computations*; Han, K., Chu, T., Eds.; RSC Publishing: Cambridge, 2014; pp 494−529.
(56) Dobbyn, A. J.; Stumpf, M.; Keller, H.-M.; Hase, W. L.; Schinke, R. *J. Chem. Phys.* **1995**, *102*, 5867−5870.
(57) Hase, W. L. *J. Phys. Chem.* **1982**, *86*, 2873−2879.
(58) Manikandan, P.; Zhang, J.; Hase, W. L. *J. Phys. Chem. A* **2012**, *116*, 3061−3080.
(59) Aoiz, F. J.; Herrero, V. J.; Sáez Rábanos, V. *J. Chem. Phys.* **1992**, *97*, 7423−7436.
(60) Schnieder, L.; Seekamp-Rahn, K.; Borkowski, J.; Wrede, E.; Welge, K. H.; Aoiz, F. J.; Bañares, L.; D'Mello, M. J.; Herrero, V. J.; Sáez Rábanos, V.; Wyatt, R. E. *Science* **1995**, *269*, 207−210.
(61) Aoiz, F. J.; Bañares, L.; Herrero, V. J. *J. Chem. Soc., Faraday Trans.* **1998**, *94*, 2483−2500.
(62) Aoiz, F. J.; Bañares, L.; Herrero, V. J.; Sáez Rábanos, V.; Stark, K.; Werner, H.-J. *J. Phys. Chem.* **1994**, *98*, 10665−10670.
(63) Martínez-Haya, B.; Aoiz, F. J.; Bañares, L.; Honvault, P.; Launay, J. M. *Phys. Chem. Chem. Phys.* **1999**, *1*, 3415−3427.
(64) Ju, L.-P.; Han, K.-L.; Zhang, J. Z. H. *J. Comput. Chem.* **2009**, *30*, 305−316.
(65) Vande Linde, S. R.; Hase, W. L. *J. Chem. Phys.* **1990**, *93*, 7962−7980.
(66) Peslherbe, G. H.; Wang, H.; Hase, W. L. *J. Chem. Phys.* **1995**, *102*, 5626−5634.
(67) Mikosch, J.; Otto, R.; Trippel, S.; Eichhorn, C.; Weidemüller, M.; Wester, R. *J. Phys. Chem. A* **2008**, *112*, 10448−10452.
(68) Li, C.; Ross, P.; Szulejko, J. E.; McMahon, T. B. *J. Am. Chem. Soc.* **1996**, *118*, 9360−9367.
(69) Xie, J.; Sun, R.; Siebert, M. R.; Otto, R.; Wester, R.; Hase, W. L. *J. Phys. Chem. A* **2013**, *117*, 7162−7178.
(70) Xie, J.; Kohale, S. C.; Hase, W. L.; Ard, S. G.; Melko, J. J.; Shuman, N. S.; Viggiano, A. A. *J. Phys. Chem. A* **2013**, *117*, 14019−14027.
(71) Fu, B.; Han, Y.-C.; Bowman, J. M.; Angelucci, L.; Balucani, N.; Leonori, F.; Casavecchia, P. *Proc. Natl. Acad. Sci. U. S. A.* **2012**, *109*, 9733−9738.
(72) Bolton, K.; Hase, W. L.; Peslherbe, G. H. In *Multidimensional Molecular Dynamics Methods*; Thompson, D. L., Ed.; World Scientific: London, 1998; pp 143−189.
(73) Sun, L.; Hase, W. L. *Rev. Comput. Chem.* **2003**, *19*, 79−146.
(74) Paranjothy, M.; Sun, R.; Zhuang, Y.; Hase, W. L. *WIREs Comput. Mol. Sci.* **2013**, *3*, 296−316.
(75) Hase, W. L. In *Encyclopedia of Computational Chemistry*, Vol. *1*; Allinger, N. L., Ed.; Wiley: New York, 1998; pp 402−407.
(76) Peslherbe, G. H.; Wang, H.; Hase, W. L. *Adv. Chem. Phys.* **1999**, *105*, 171−201.
(77) Bolton, K.; Hase, W. L. In *Encyclopedia of Computational Chemistry*, Vol. *2*; Allinger, N. L., Ed.; Wiley: New York, 1998; pp 1347−1360.
(78) Hase, W. L. In *Encyclopedia of Computational Chemistry*, Vol. *1*; Allinger, N. L.; Wiley: New York, 1998; pp 399−402.
(79) Li, G.; Hase, W. L. *J. Am. Chem. Soc.* **1999**, *121*, 7124−7129.
(80) Lourderaj, U.; Sun, R.; Kohale, S. C.; Barnes, G. L.; de Jong, W. A.; Windus, T. L.; Hase, W. L. *Comput. Phys. Commun.* **2014**, *185*, 1074−1080.
(81) Helgaker, T.; Uggerud, E.; Jensen, Aa. *Chem. Phys. Lett.* **1990**, *173*, 145−150.
(82) Uggerud, E.; Helgaker, T. *J. Am. Chem. Soc.* **1992**, *114*, 4265−4268.
(83) Chen, W.; Hase, W. L.; Schlegel, H. B. *Chem. Phys. Lett.* **1994**, *228*, 436−442.
(84) Millam, J. M.; Bakken, V.; Chen, W.; Hase, W. L.; Schlegel, H. B. *J. Chem. Phys.* **1999**, *111*, 3800−3805.
(85) Lourderaj, U.; Song, K.; Windus, T. L.; Zhuang, Y.; Hase, W. L. *J. Chem. Phys.* **2007**, *126*, 044105.
(86) Hurd, P.; Cusati, T.; Persico, M. *J. Comput. Phys.* **2010**, *229*, 2109−2116.
(87) Bofill, J. M. *J. Comput. Chem.* **1994**, *15*, 1−11.
(88) Bakken, V.; Millam, J. M.; Schlegel, H. B. *J. Chem. Phys.* **1999**, *111*, 8773−8777.
(89) Wu, H.; Rahman, M.; Wang, J.; Louderaj, U.; Hase, W. L.; Zhuang, Y. *J. Chem. Phys.* **2010**, *133*, 074101.
(90) Zhuang, Y.; Siebert, M. R.; Hase, W. L.; Kay, K. G.; Ceotto, M. *J. Chem. Theory Comput.* **2013**, *9*, 54−64.
(91) Xie, J.; Otto, R.; Mikosch, J.; Zhang, J.; Wester, R.; Hase, W. L. *Acc. Chem. Res.* **2014**, *47*, 2960−2969.
(92) Xie, J.; Hase, W. L. *Science* **2016**, *352*, 32−33.
(93) Mikosch, J.; Trippel, S.; Eichhorn, C.; Otto, R.; Lourderaj, U.; Zhang, J. X.; Hase, W. L.; Weidemüller, M.; Wester, R. *Science* **2008**, *319*, 183−186.
(94) Olmstead, W. M.; Brauman, J. I. *J. Am. Chem. Soc.* **1977**, *99*, 4219−4228.
(95) Vande Linde, S. R.; Hase, W. L. *J. Am. Chem. Soc.* **1989**, *111*, 2349−2351.
(96) Vande Linde, S. R.; Hase, W. L. *J. Phys. Chem.* **1990**, *94*, 6148−6150.
(97) Hase, W. L. *Science* **1994**, *266*, 998−1002.
(98) Zhang, J.; Lourderaj, U.; Sun, R.; Mikosch, J.; Wester, R.; Hase, W. L. *J. Chem. Phys.* **2013**, *138*, 114309.
(99) Wang, Y.; Hase, W. L.; Wang, H. *J. Chem. Phys.* **2003**, *118*, 2688−2695.
(100) Zhang, J.; Mikosch, J.; Trippel, S.; Otto, R.; Weidemüller, M.; Wester, R.; Hase, W. L. *J. Phys. Chem. Lett.* **2010**, *1*, 2747−2752.
(101) Mikosch, J.; Zhang, J.; Trippel, S.; Eichhorn, C.; Otto, R.; Sun, R.; de Jong, W. A.; Weidemüller, M.; Hase, W. L.; Wester, R. *J. Am. Chem. Soc.* **2013**, *135*, 4250−4259.
(102) Sun, R.; Davda, C. J.; Zhang, J.; Hase, W. L. *Phys. Chem. Chem. Phys.* **2015**, *17*, 2589−2597.
(103) Sun, R.; Xie, J.; Zhang, J.; Hase, W. L. *Int. J. Mass Spectrom.* **2015**, *377*, 222−227.
(104) Zhang, J.; Xie, J.; Hase, W. L. *J. Phys. Chem. A* **2015**, *119*, 12517−12525.
(105) Otto, R.; Xie, J.; Brox, J.; Trippel, S.; Stei, M.; Best, T.; Siebert, M. R.; Hase, W. L.; Wester, R. *Faraday Discuss.* **2012**, *157*, 41−57.
(106) Xie, J.; Otto, R.; Wester, R.; Hase, W. L. *J. Chem. Phys.* **2015**, *142*, 244308.
(107) Xie, J.; Scott, M. J.; Hase, W. L.; Hierl, P. M.; Viggiano, A. A. *Z. Phys. Chem.* **2015**, *229*, 1747−1763.
(108) Xie, J.; McClellan, M.; Sun, R.; Kohale, S. C.; Govind, N.; Hase, W. L. *J. Phys. Chem. A* **2015**, *119*, 817−825.
(109) Zhang, J.; Yang, L.; Xie, J.; Hase, W. L. *J. Phys. Chem. Lett.* **2016**, *7*, 660−665.
(110) Schmatz, S.; Botschwina, P.; Hauschildt, J.; Schinke, R. *J. Chem. Phys.* **2002**, *117*, 9710−9718.
(111) Schmatz, S. *J. Chem. Phys.* **2005**, *122*, 234306.
(112) Wang, Y.; Song, K.; Hase, W. L. *J. Am. Soc. Mass Spectrom.* **2003**, *14*, 1402−1412.
(113) Park, K.; Deb, B.; Song, K.; Hase, W. L. *J. Am. Soc. Mass Spectrom.* **2009**, *20*, 939−948.
(114) Yang, L.; Sun, R.; Hase, W. L. *Comput. Theor. Chem.* **2012**, *990*, 62−66.

DOI: 10.1021/jacs.6b12017
J. Am. Chem. Soc. 2017, 139, 3570−3590

(115) Homayoon, Z.; Pratihar, S.; Dratz, E.; Snider, R.; Spezia, R.; Barnes, G. L.; Macaluso, V.; Martin Somer, A.; Hase, W. L. *J. Phys. Chem. A* **2016**, *120*, 8211−8227.
(116) Carpenter, B. K. *J. Am. Chem. Soc.* **1995**, *117*, 6336−6344.
(117) Doubleday, C., Jr.; Bolton, K.; Peslherbe, G. H.; Hase, W. L. *J. Am. Chem. Soc.* **1996**, *118*, 9922−9931.
(118) Doubleday, C., Jr.; Bolton, K.; Hase, W. L. *J. Am. Chem. Soc.* **1997**, *119*, 5251−5252.
(119) Doubleday, C., Jr.; Bolton, K.; Hase, W. L. *J. Phys. Chem. A* **1998**, *102*, 3648−3658.
(120) Carpenter, B. K. *J. Am. Chem. Soc.* **1996**, *118*, 10329−10330.
(121) Doubleday, C., Jr.; Li, G.; Hase, W. L. *Phys. Chem. Chem. Phys.* **2002**, *4*, 304−312.
(122) Debbert, S. L.; Carpenter, B. K.; Hrovat, D. A.; Borden, W. T. *J. Am. Chem. Soc.* **2002**, *124*, 7896−7897.
(123) Nummela, J. A.; Carpenter, B. K. *J. Am. Chem. Soc.* **2002**, *124*, 8512−8513.
(124) Vayner, G.; Addepalli, S. V.; Song, K.; Hase, W. L. *J. Chem. Phys.* **2006**, *125*, 014317.
(125) Litovitz, A. E.; Keresztes, I.; Carpenter, B. K. *J. Am. Chem. Soc.* **2008**, *130*, 12085−12094.
(126) Kakhiani, K.; Lourderaj, U.; Hu, W.; Birney, D. M.; Hase, W. L. *J. Phys. Chem. A* **2009**, *113*, 4570−4580.
(127) Oyola, Y.; Singleton, D. A. *J. Am. Chem. Soc.* **2009**, *131*, 3130−3131.
(128) Goldman, L. M.; Glowacki, D. R.; Carpenter, B. K. *J. Am. Chem. Soc.* **2011**, *133*, 5312−5313.
(129) Quijano, L. M. M.; Singleton, D. A. *J. Am. Chem. Soc.* **2011**, *133*, 13824−13827.
(130) Sun, R.; Park, K.; de Jong, W. A.; Lischka, H.; Windus, T. L.; Hase, W. L. *J. Chem. Phys.* **2012**, *137*, 044305.
(131) Paranjothy, M.; Siebert, M. A.; Hase, W. L.; Bachrach, S. M. *J. Phys. Chem. A* **2012**, *116*, 11492−11499.
(132) Sun, R.; Siebert, M. R.; Xu, L.; Chambreau, S. D.; Vaghjiani, G. L.; Lischka, H.; Liu, J.; Hase, W. L. *J. Phys. Chem. A* **2014**, *118*, 2228−2236.
(133) Chen, Z.; Nieves-Quinones, Y.; Waas, J. R.; Singleton, D. A. *J. Am. Chem. Soc.* **2014**, *136*, 13122−13125.
(134) Osterheld, T. H.; Brauman, J. I. *J. Am. Chem. Soc.* **1993**, *115*, 10311−10316.
(135) Lourderaj, U.; McAfee, J. L.; Hase, W. L. *J. Chem. Phys.* **2008**, *129*, 094701.
(136) McQuarrie, D. A. *Statistical Thermodynamics*; Harper: New York, 1973.
(137) Baer, T.; Hase, W. L. *Unimolecular Reaction Dynamics. Theory and Experiments*; Oxford: New York, 1996; p 328.
(138) Steinfeld, J. I.; Francisco, J. S.; Hase, W. L. *Chemical Kinetics and Dynamics*, 2nd ed.; Prentice-Hall: New York, 1999.
(139) Yang, L.; Sun, R.; Hase, W. L. *J. Chem. Theory Comput.* **2011**, *7*, 3478−3483.
(140) Li, X.; Millam, J. M.; Schlegel, H. B. *J. Chem. Phys.* **2000**, *113*, 10062−10067.
(141) Bowman, J. M. *Mol. Phys.* **2014**, *112*, 2516−2528.
(142) Sun, L.; Hase, W. L. *J. Chem. Phys.* **2004**, *121*, 8831−8845.
(143) Dong, E.; Setser, D. W.; Hase, W. L.; Song, K. *J. Phys. Chem. A* **2006**, *110*, 1484−1490.
(144) Sun, L.; Park, K.; Song, K.; Setser, D. W.; Hase, W. L. *J. Chem. Phys.* **2006**, *124*, 064313.
(145) Arunan, E.; Wategaonkar, S. J.; Setser, D. W. *J. Phys. Chem.* **1991**, *95*, 1539−1547.
(146) Quick, C. R., Jr.; Wittig, C. *J. Chem. Phys.* **1980**, *72*, 1694−1700.
(147) Zamir, E.; Levine, R. D. *Chem. Phys.* **1980**, *52*, 253−268.
(148) Xu, L.; Doubleday, C. E.; Houk, K. N. *Angew. Chem., Int. Ed.* **2009**, *48*, 2746−2748.
(149) Barnes, G. L.; Hase, W. L. *Nat. Chem.* **2009**, *1*, 103−104.
(150) Thomas, J. B.; Waas, J. R.; Harmata, M.; Singleton, D. A. *J. Am. Chem. Soc.* **2008**, *130*, 14544−14555.
(151) Siebert, M. R.; Zhang, J.; Addepalli, S. V.; Tantillo, D. J.; Hase, W. L. *J. Am. Chem. Soc.* **2011**, *133*, 8335−8343.
(152) Siebert, M. R.; Manikandan, P.; Sun, R.; Tantillo, D. J.; Hase, W. L. *J. Chem. Theory Comput.* **2012**, *8*, 1212−1222.
(153) Quapp, W.; Bofill, J. *J. Math. Chem.* **2012**, *50*, 2061−2085.
(154) Collins, P.; Carpenter, B. K.; Ezra, G. S.; Wiggins, S. *J. Chem. Phys.* **2013**, *139*, 154108.
(155) Kramer, Z. C.; Carpenter, B. K.; Ezra, G. S.; Wiggins, S. *J. Phys. Chem. A* **2015**, *119*, 6611−6630.
(156) Mann, D. J.; Hase, W. L. *J. Am. Chem. Soc.* **2002**, *124*, 3208−3209.
(157) Martín-Sómer, A.; Yáñez, M.; Hase, W. L.; Gaigeot, M.-P.; Spezia, R. *J. Chem. Theory Comput.* **2016**, *12*, 974−982.
(158) Black, K.; Liu, P.; Doubleday, C.; Houk, K. N. *Proc. Natl. Acad. Sci. U. S. A.* **2012**, *109*, 12860−12865.
(159) Yang, Z.; Doubleday, C.; Houk, K. N. *J. Chem. Theory Comput.* **2015**, *11*, 5606−5612.
(160) Ammal, S. C.; Yamataka, H.; Aida, M.; Dupuis, M. *Science* **2003**, *299*, 1555−1557.
(161) Marcy, T. P.; Díaz, R. R.; Heard, D.; Leone, S. R.; Harding, L. B.; Klippenstein, S. J. *J. Phys. Chem. A* **2001**, *105*, 8361−8369.
(162) Sun, L.; Song, K.; Hase, W. L. *Science* **2002**, *296*, 875−878.
(163) López, J. G.; Vayner, G.; Lourderaj, U.; Addepalli, S. V.; Kato, S.; deJong, W. A.; Windus, T. L.; Hase, W. L. *J. Am. Chem. Soc.* **2007**, *129*, 9976−9985.
(164) Blanksby, S. J.; Ellison, G. B.; Bierbaum, B. V.; Kato, S. *J. Am. Chem. Soc.* **2002**, *124*, 3196.
(165) Cho, Y. J.; Vande Linde, S. R.; Zhu, L.; Hase, W. L. *J. Chem. Phys.* **1992**, *96*, 8275−8287.
(166) Sun, L.; Hase, W. L.; Song, K. *J. Am. Chem. Soc.* **2001**, *123*, 5753−5756.
(167) Cheon, S.; Song, K.; Hase, W. L. *J. Mol. Struct.: THEOCHEM* **2006**, *771*, 27−31.
(168) Sun, L.; Chang, E.; Song, K.; Hase, W. L. *Can. J. Chem.* **2004**, *82*, 891−899.
(169) Yu, F. *J. Comput. Chem.* **2012**, *33*, 401−405.
(170) Pratihar, S.; Barnes, G.; Hase, W. L. *Chem. Soc. Rev.* **2016**, *45*, 3595−3608.
(171) Pratihar, S.; Barnes, G. L.; Laskin, J.; Hase, W. L. *J. Phys. Chem. Lett.* **2016**, *7*, 3142−3150.
(172) Meroueh, S. O.; Wang, Y.; Hase, W. L. *J. Phys. Chem. A* **2002**, *106*, 9983−9992.
(173) Park, K.; Song, K.; Hase, W. L. *Int. J. Mass Spectrom.* **2007**, *265*, 326−336.
(174) Wang, J.; Meroueh, S. O.; Wang, Y.; Hase, W. L. *Int. J. Mass Spectrom.* **2003**, *230*, 57−64.
(175) Laskin, J.; Denisov, E.; Futrell, J. *J. Am. Chem. Soc.* **2000**, *122*, 9703−9714.
(176) Laskin, J.; Futrell, J. H. *J. Chem. Phys.* **2003**, *119*, 3413−3420.
(177) Barnes, G. L.; Hase, W. L. *J. Am. Chem. Soc.* **2009**, *131*, 17185−17193.
(178) Meroueh, O.; Hase, W. L. *J. Am. Chem. Soc.* **2002**, *124*, 1524−1531.
(179) Laskin, J.; Bailey, T. H.; Futrell, J. H. *J. Am. Chem. Soc.* **2003**, *125*, 1625−1632.
(180) Laskin, J.; Futrell, J. H. *J. Am. Soc. Mass Spectrom.* **2003**, *14*, 1340−1347.
(181) Barnes, G. L.; Young, K.; Yang, L.; Hase, W. L. *J. Chem. Phys.* **2011**, *134*, 094106.
(182) Geragotelis, A.; Barnes, G. L. *J. Phys. Chem. C* **2013**, *117*, 13087−13093.
(183) Wysocki, V. H.; Tsaprailis, G.; Smith, L. L.; Breci, L. A. *J. Mass Spectrom.* **2000**, *35*, 1399−1406.
(184) Wysocki, V. H.; Cheng, G.; Zhang, Q.; Hermann, K. A.; Beardsley, R. L.; Hilderbrand, A. E. In *Principles of Mass Spectrometry Applied to Biomolecules*; Laskin, J., Lifshitz, C., Eds.; John Wiley and Sons: Hoboken, NJ, 2006; Chapter VIII, pp 279−300.
(185) Gregg, Z.; Ijaz, W.; Jannetti, S.; Barnes, G. L. *J. Phys. Chem. C* **2014**, *118*, 22149−22155.

DOI: 10.1021/jacs.6b12017
J. Am. Chem. Soc. 2017, 139, 3570−3590

(186) Ijaz, W.; Gregg, Z.; Barnes, G. L. *J. Phys. Chem. Lett.* **2013**, *4*, 3935−3939.
(187) Shaikh, K.; Blackwood, J.; Barnes, G. L. *Chem. Phys. Lett.* **2015**, *637*, 83−87.
(188) Wang, P.; Hadjar, O.; Gassman, P. L.; Laskin, J. *Phys. Chem. Chem. Phys.* **2008**, *10*, 1512−1522.
(189) Spezia, R.; Salpin, J.-Y.; Gaigeot, M.-P; Hase, W. L.; Song, K. *J. Phys. Chem. A* **2009**, *113*, 13853−13862.
(190) Jeanvoine, Y.; Gaigeot, M.-P.; Hase, W. L.; Song, K.; Spezia, R. *Int. J. Mass Spectrom.* **2011**, *308*, 289−298.
(191) Spezia, R.; Cimas, A.; Gaigeot, M.-P.; Salpin, J.-Y.; Song, K.; Hase, W. L. *Phys. Chem. Chem. Phys.* **2012**, *14*, 11724−11736.
(192) Ortiz, D.; Martin-Gago, P.; Riera, A.; Song, K.; Salpin, J.-Y.; Spezia, R. *Int. J. Mass Spectrom.* **2013**, *335*, 33−44.
(193) Ortiz, D.; Salpin, J.-Y.; Song, K.; Spezia, R. *Int. J. Mass Spectrom.* **2014**, *358*, 25−35.
(194) Martin-Somer, A.; Yanez, M.; Gaigeot, M.-P.; Spezia, R. *J. Phys. Chem. A* **2014**, *118*, 10882−10893.
(195) Spezia, R.; Martens, J.; Oomens, J.; Song, K. *Int. J. Mass Spectrom.* **2015**, *388*, 40−52.
(196) Rossich Molina, E.; Ortiz, D.; Salpin, J.-Y.; Spezia, R. *J. Mass Spectrom.* **2015**, *50*, 1340−1351.
(197) Spezia, R.; Lee, S. B.; Cho, A.; Song, K. *Int. J. Mass Spectrom.* **2015**, *392*, 125−138.
(198) Rossich Molina, E.; Salpin, J.-Y.; Spezia, R.; Martínez-Núñez, E. *Phys. Chem. Chem. Phys.* **2016**, *18*, 14980−14990.
(199) Spezia, R.; Martin-Somer, A.; Macaluso, V.; Homayoon, Z.; Pratihar, S.; Hase, W. L. *Faraday Discuss.* **2016**, *195*, 599−618.
(200) Lee, G.; Park, E.; Chung, H.; Jeanvoine, Y.; Song, K.; Spezia, R. *Int. J. Mass Spectrom.* **2016**, *407*, 40−50.
(201) Gaigeot, M.-P.; Spezia, R. *Top. Curr. Chem.* **2014**, *364*, 99−151.
(202) Zhuang, Y.; Siebert, M. R.; Hase, W. L.; Kay, K. G.; Ceotto, M. *J. Chem. Theory Comput.* **2013**, *9*, 54−64.
(203) Ceotto, M.; Zhuang, Y.; Hase, W. L. *J. Chem. Phys.* **2013**, *138*, 054116.
(204) Miller, W. H. *Adv. Chem. Phys.* **1974**, *25*, 69−177.
(205) Heller, E. J. *J. Chem. Phys.* **1975**, *62*, 1544−1555.
(206) Herman, M. F.; Kluk, E. *Chem. Phys.* **1984**, *91*, 27−34.
(207) Kay, K. G. *J. Chem. Phys.* **1994**, *100*, 4432−4445.
(208) Kaledin, A. L.; Miller, W. H. *J. Chem. Phys.* **2003**, *119*, 3078−3084.
(209) Ceotto, M.; Atahan, S.; Tantardini, G. F.; Aspuru-Guzik, A. *J. Chem. Phys.* **2009**, *130*, 234113.
(210) Ceotto, M.; Dell'Angelo, D.; Tantardini, G. F. *J. Chem. Phys.* **2010**, *133*, 054701.
(211) Tully, J. C. *J. Chem. Phys.* **1990**, *93*, 1061−1071.
(212) Hammes-Schiffer, S.; Tully, J. C. *J. Chem. Phys.* **1994**, *101*, 4657−4667.
(213) Barbatti, M.; Aquino, A. J. A.; Szymczak, J. J.; Nachtigallová, D.; Hobza, P.; Lischka, H. *Proc. Natl. Acad. Sci. U. S. A.* **2010**, *107*, 21453−21458.
(214) Yang, S.; Martinez, T. J. In *Conical Intersections: Theory, Computation and Experiment*; Domcke, W., Koppel, H., Eds.; World Scientific: Singapore, 2011.
(215) Tuna, D.; Sobolewski, A. L.; Domcke, W. *J. Phys. Chem. B* **2016**, *120*, 10729−10735.
(216) Ruckenbauer, M.; Barbatti, M.; Müller, T.; Lischka, H. *J. Phys. Chem. A* **2013**, *117*, 2790−2799.
(217) Liu, L.; Liu, J.; Martinez, T. J. *J. Phys. Chem. B* **2016**, *120*, 1940−1949.
(218) Plasser, F.; Crespo-Otero, R.; Pederzoli, M.; Pittner, J.; Lischka, H.; Barbatti, M. *J. Chem. Theory Comput.* **2014**, *10*, 1395−1405.
(219) Tuna, D.; Došlić, N.; Mališ, M.; Sobolewski, A. L.; Domcke, W. *J. Phys. Chem. B* **2015**, *119*, 2112−2124.
(220) Lu, Y.; Lan, Z.; Thiel, W. *Angew. Chem., Int. Ed.* **2011**, *50*, 6864−6867.
(221) Cui, G.; Lan, Z.; Thiel, W. *J. Am. Chem. Soc.* **2012**, *134*, 1662−1672.
(222) Liu, X.-Y.; Chang, X.-P.; Xia, S.-H; Cui, G.; Thiel, W. *J. Chem. Theory Comput.* **2016**, *12*, 753−764.
(223) Mardirossian, N.; Head-Gordon, M. *Phys. Chem. Chem. Phys.* **2014**, *16*, 9904−9924.
(224) Yu, H. S.; He, X.; Li, S. L.; Truhlar, D. *Chem. Sci.* **2016**, *7*, 5032−5051.

DOI: 10.1021/jacs.6b12017
J. Am. Chem. Soc. 2017, 139, 3570−3590